A Search for Pulsars around Sgr A* in the First Event Horizon Telescope Data Set

The Astrophysical Journal, 959:14 (27pp), 2023 December 10 https://doi.org/10.3847/1538-4357/acf4f2

A Search for Pulsars around Sgr A* in the First Event Horizon Telescope Data Set

Pablo Torne[1,2], Kuo Liu[2], Ralph P. Eatough[3,2], Jompoj Wongphechauxsorn[2], James M. Cordes[4], Gregory Desvignes[2,5], Mariafelicia De Laurentis[6,7,8], Michael Kramer[2,9], Scott M. Ransom[10], Shami Chatterjee[4], Robert Wharton[11], Ramesh Karuppusamy[2], Lindy Blackburn[12,13], Michael Janssen[2], Chi-kwan Chan[14,15,16], Geoffrey, B. Crew[17], Lynn D. Matthews[17], Ciriaco Goddi[18,19,20,21], Helge Rottmann[2], Jan Wagner[2], Salvador Sánchez[1], Ignacio Ruiz[1], Federico Abbate[2], Geoffrey C. Bower[22,23], Juan J. Salamanca[24], Arturo I. Gómez-Ruiz[25,26], Alfredo Herrera-Aguilar[27], Wu Jiang (江悟)[28], Ru-Sen Lu (路如森)[28,29,2], Ue-Li Pen[30,31,32,33,34], Alexander W. Raymond[12,13], Lijing Shao[35,2], Zhiqiang Shen (沈志强)[28,29], Gabriel Paubert[1], Miguel Sanchez-Portal[1], Carsten Kramer[36], Manuel Castillo[1], Santiago Navarro[1], David John[1], Karl-Friedrich Schuster[36], Michael D. Johnson[12,13], Kazi L. J. Rygl[37], Kazunori Akiyama[17,38,12], Antxon Alberdi[39], Walter Alef[2], Juan Carlos Algaba[40], Richard Anantua[12,13,41], Keiichi Asada[30], Rebecca Azulay[42,43,2], Uwe Bach[2], Anne-Kathrin Baczko[44,2], David Ball[14], Mislav Baloković[45], John Barrett[17], Michi Bauböck[46], Bradford A. Benson[47,48], Dan Bintley[49,50], Raymond Blundell[13], Katherine L. Bouman[51], Hope Boyce[52,53], Michael Bremer[36], Christiaan D. Brinkerink[54], Roger Brissenden[12,13], Silke Britzen[2], Avery E. Broderick[31,55,56], Dominique Broguiere[36], Thomas Bronzwaer[54], Sandra Bustamante[57], Do-Young Byun[58,59], John E. Carlstrom[60,48,61,62], Chiara Ceccobello[44], Andrew Chael[63], Dominic O. Chang[12,13], Koushik Chatterjee[12,13], Ming-Tang Chen[22], Yongjun Chen (陈永军)[28,29], Xiaopeng Cheng[58], Ilje Cho[39], Pierre Christian[64], Nicholas S. Conroy[65,13], John E. Conway[44], Thomas M. Crawford[48,60], Alejandro Cruz-Osorio[7], Yuzhu Cui (崔玉竹)[66,67], Rohan Dahale[39], Jordy Davelaar[68,69,54], Roger Deane[70,71,72], Jessica Dempsey[49,50,73], Jason Dexter[74], Vedant Dhruv[46], Sheperd S. Doeleman[12,13], Sean Dougal[14], Sergio A. Dzib[36,2], Razieh Emami[13], Heino Falcke[54], Joseph Farah[75,76], Vincent L. Fish[17], Ed Fomalont[10], H. Alyson Ford[14], Marianna Foschi[39], Raquel Fraga-Encinas[54], William T. Freeman[77,78], Per Friberg[49,50], Christian M. Fromm[79,7,2], Antonio Fuentes[39], Peter Galison[12,80,81], Charles F. Gammie[46,65,82], Roberto García[36], Olivier Gentaz[36], Boris Georgiev[55,56,31], Roman Gold[83], José L. Gómez[39], Minfeng Gu (顾敏峰)[28,84], Mark Gurwell[13], Kazuhiro Hada[85,86], Daryl Haggard[52,53], Kari Haworth[13], Michael H. Hecht[17], Ronald Hesper[87], Dirk Heumann[14], Luis C. Ho (何子山)[88,35], Paul Ho[30,50,49], Mareki Honma[85,86,89], Chih-Wei L. Huang[30], Lei Huang (黄磊)[28,84], David H. Hughes[25], Shiro Ikeda[38,90,91,92], C. M. Violette Impellizzeri[93,10], Makoto Inoue[30], Sara Issaoun[13,154], David J. James[94,95], Buell T. Jannuzi[14], Britton Jeter[30], Alejandra Jiménez-Rosales[54], Svetlana Jorstad[96], Abhishek V. Joshi[46], Taehyun Jung[58,59], Mansour Karami[31,55], Tomohisa Kawashima[97], Garrett K. Keating[13], Mark Kettenis[98], Dong-Jin Kim[2], Jae-Young Kim[99,2], Jongsoo Kim[58], Junhan Kim[51], Motoki Kino[38,100], Jun Yi Koay[30], Prashant Kocherlakota[7], Yutaro Kofuji[85,89], Shoko Koyama[101,30], Thomas P. Krichbaum[2], Cheng-Yu Kuo[102,30], Noemi La Bella[54], Tod R. Lauer[103], Daeyoung Lee[46], Sang-Sung Lee[58], Po Kin Leung[104], Aviad Levis[51], Zhiyuan Li (李志远)[105,106], Rocco Lico[39,107], Greg Lindahl[13], Michael Lindqvist[44], Mikhail Lisakov[2], Jun Liu (刘俊)[2], Elisabetta Liuzzo[37], Wen-Ping Lo[30,108], Andrei P. Lobanov[2], Laurent Loinard[109,110], Colin J. Lonsdale[17], Nicholas R. MacDonald[2], Jirong Mao (毛基荣)[111,112,113], Nicola Marchili[37,2], Sera Markoff[114,115], Daniel P. Marrone[14], Alan P. Marscher[96], Iván Martí-Vidal[42,43], Satoki Matsushita[30], Lia Medeiros[116,14], Karl M. Menten[2], Daniel Michalik[117,48], Izumi Mizuno[49,50], Yosuke Mizuno[67,118,7], James M. Moran[12,13], Kotaro Moriyama[7,17,85], Monika Moscibrodzka[54], Cornelia Müller[2,54], Hendrik Müller[2], Alejandro Mus[42,43], Gibwa Musoke[114,54], Ioannis Myserlis[1], Andrew Nadolski[65], Hiroshi Nagai[38,86], Neil M. Nagar[119], Masanori Nakamura[120,30], Ramesh Narayan[12,13], Gopal Narayanan[57], Iniyan Natarajan[13,12], Antonios Nathanail[121,7], Joey Neilsen[122], Roberto Neri[36], Chunchong Ni[55,56,31], Aristeidis Noutsos[2], Michael A. Nowak[123], Junghwan Oh[124], Hiroki Okino[85,89], Héctor Olivares[54], Gisela N. Ortiz-León[110,2], Tomoaki Oyama[85], Feryal Özel[125], Daniel C. M. Palumbo[12,13], Georgios Filippos Paraschos[2], Jongho Park[58,30], Harriet Parsons[49,50], Nimesh Patel[13], Dominic W. Pesce[13,12], Vincent Piétu[36], Richard Plambeck[126], Aleksandar PopStefanija[57], Oliver Porth[114,7], Felix M. Pötzl[127,2], Ben Prather[46], Jorge A. Preciado-López[31], Dimitrios Psaltis[125], Hung-Yi Pu[128,129,30], Venkatessh Ramakrishnan[119,130,131], Ramprasad Rao[13], Mark G. Rawlings[132,49,50], Luciano Rezzolla[7,133,134], Angelo Ricarte[13,12], Bart Ripperda[116,154,135,69], Freek Roelofs[12,13,54], Alan Rogers[17], Eduardo Ros[2], Cristina Romero-Cañizales[30], Arash Roshanineshat[14], Alan L. Roy[2], Chet Ruszczyk[17], David Sánchez-Argüelles[25,26], Mahito Sasada[136,85,137], Kaushik Satapathy[14], Tuomas Savolainen[138,131,2], F. Peter Schloerb[57], Jonathan Schonfeld[13], Des Small[98], Bong Won Sohn[58,59,139], Jason SooHoo[17], Kamal Souccar[57], He Sun (孙赫)[51], Alexandra J. Tetarenko[140], Paul Tiede[13,12], Remo P. J. Tilanus[14,54,93,141], Michael Titus[17], Teresa Toscano[39], Efthalia Traianou[39,2], Tyler Trent[14], Sascha Trippe[142], Matthew Turk[65], Ilse van Bemmel[98], Huib Jan van Langevelde[93,98,143], Daniel R. van Rossum[54], Jesse Vos[54], Derek Ward-Thompson[144], John Wardle[145], Jonathan Weintroub[12,13],

Norbert Wex[2], Maciek Wielgus[2], Kaj Wiik[146], Gunther Witzel[2], Michael F. Wondrak[54,147], George N. Wong[116,148], Qingwen Wu (吴庆文)[149], Nitika Yadlapalli[51], Paul Yamaguchi[13], Aristomenis Yfantis[54], Doosoo Yoon[114], André Young[54], Ken Young[13], Ziri Younsi[150,7], Wei Yu (于威)[13], Feng Yuan (袁峰)[28,84,151], Ye-Fei Yuan (袁业飞)[152], J. Anton Zensus[2], Shuo Zhang[153], Guang-Yao Zhao[39], and Shan-Shan Zhao (赵杉杉)[28]

[1] Institut de Radioastronomie Millimétrique, Avenida Divina Pastora 7, Local 20, E-18012, Granada, Spain; torne@iram.es
[2] Max-Planck-Institut für Radioastronomie, Auf dem Hügel 69, D-53121 Bonn, Germany; kliu@mpifr-bonn.mpg.de
[3] National Astronomical Observatories, Chinese Academy of Sciences, 20A Datun Road, Chaoyang District, Beijing 100101, People's Republic of China
[4] Cornell Center for Astrophysics and Planetary Science, Cornell University, Ithaca, NY 14853, USA
[5] LESIA, Observatoire de Paris, Université PSL, CNRS, Sorbonne Université, Université de Paris, 5 place Jules Janssen, F-92195 Meudon, France
[6] Dipartimento di Fisica "E. Pancini,"Università di Napoli "Federico II," Compl. Univ. di Monte S. Angelo, Edificio G, Via Cinthia, I-80126, Napoli, Italy
[7] Institut für Theoretische Physik, Goethe-Universität Frankfurt, Max-von-Laue-Straße 1, D-60438 Frankfurt am Main, Germany
[8] INFN Sez. di Napoli, Compl. Univ. di Monte S. Angelo, Edificio G, Via Cinthia, I-80126, Napoli, Italy
[9] Jodrell Bank Centre for Astrophysics, School of Physics and Astronomy, The University of Manchester, Manchester M13 9PL, UK
[10] National Radio Astronomy Observatory, 520 Edgemont Road, Charlottesville, VA 22903, USA
[11] Jet Propulsion Laboratory, California Institute of Technology, Pasadena, CA 91109, USA
[12] Black Hole Initiative at Harvard University, 20 Garden Street, Cambridge, MA 02138, USA
[13] Center for Astrophysics | Harvard & Smithsonian, 60 Garden Street, Cambridge, MA 02138, USA
[14] Steward Observatory and Department of Astronomy, University of Arizona, 933 N. Cherry Avenue, Tucson, AZ 85721, USA
[15] Data Science Institute, University of Arizona, 1230 N. Cherry Avenue, Tucson, AZ 85721, USA
[16] Program in Applied Mathematics, University of Arizona, 617 N. Santa Rita, Tucson, AZ 85721, USA
[17] Massachusetts Institute of Technology Haystack Observatory, 99 Millstone Road, Westford, MA 01886, USA
[18] Instituto de Astronomia, Geofísica e Ciências Atmosféricas, Universidade de São Paulo, R. do Matão, 1226, São Paulo, SP 05508-090, Brazil
[19] Dipartimento di Fisica, Università degli Studi di Cagliari, SP Monserrato-Sestu km 0.7, I-09042 Monserrato (CA), Italy
[20] INAF—Osservatorio Astronomico di Cagliari, via della Scienza 5, I-09047 Selargius (CA), Italy
[21] INFN, sezione di Cagliari, I-09042 Monserrato (CA), Italy
[22] Institute of Astronomy and Astrophysics, Academia Sinica, 645 N. A'ohoku Place, Hilo, HI 96720, USA
[23] Department of Physics and Astronomy, University of Hawaii at Manoa, 2505 Correa Road, Honolulu, HI 96822, USA
[24] Departamento de Estadística e I.O., Escuela Politécnica de Ingeniería, Universidad de Oviedo, E-33071 Gijón, Spain
[25] Instituto Nacional de Astrofísica, Óptica y Electrónica. Apartado Postal 51 y 216, 72000. Puebla Pue., México
[26] Consejo Nacional de Ciencia y Tecnologìa, Av. Insurgentes Sur 1582, 03940, Ciudad de México, México
[27] Instituto de Física, Benemérita Universidad Autónoma de Puebla, Edificio IF-1, Ciudad Universitaria, CP 72570, Puebla, México
[28] Shanghai Astronomical Observatory, Chinese Academy of Sciences, 80 Nandan Road, Shanghai 200030, People's Republic of China
[29] Key Laboratory of Radio Astronomy, Chinese Academy of Sciences, Nanjing 210008, People's Republic of China
[30] Institute of Astronomy and Astrophysics, Academia Sinica, 11F of Astronomy-Mathematics Building, AS/NTU No. 1, Sec. 4, Roosevelt Road, Taipei 10617, Taiwan, R.O.C.
[31] Perimeter Institute for Theoretical Physics, 31 Caroline Street North, Waterloo, ON N2L 2Y5, Canada
[32] Canadian Institute for Theoretical Astrophysics, University of Toronto, 60 St. George Street, Toronto, ON M5S 3H8, Canada
[33] Dunlap Institute for Astronomy and Astrophysics, University of Toronto, 50 St. George Street, Toronto, ON M5S 3H4, Canada
[34] Canadian Institute for Advanced Research, 180 Dundas Street West, Toronto, ON M5G 1Z8, Canada
[35] Kavli Institute for Astronomy and Astrophysics, Peking University, Beijing 100871, People's Republic of China
[36] Institut de Radioastronomie Millimétrique, 300 rue de la Piscine, F-38406 Saint Martin d'Hères, France
[37] INAF-Istituto di Radioastronomia & Italian ALMA Regional Centre, Via P. Gobetti 101, I-40129 Bologna, Italy
[38] National Astronomical Observatory of Japan, 2-21-1 Osawa, Mitaka, Tokyo 181-8588, Japan
[39] Instituto de Astrofísica de Andalucía-CSIC, Glorieta de la Astronomía s/n, E-18008 Granada, Spain
[40] Department of Physics, Faculty of Science, Universiti Malaya, 50603 Kuala Lumpur, Malaysia
[41] Department of Physics & Astronomy, The University of Texas at San Antonio, One UTSA Circle, San Antonio, TX 78249, USA
[42] Departament d'Astronomia i Astrofísica, Universitat de València, C. Dr. Moliner 50, E-46100 Burjassot, València, Spain
[43] Observatori Astronòmic, Universitat de València, C. Catedrático José Beltrán 2, E-46980 Paterna, València, Spain
[44] Department of Space, Earth and Environment, Chalmers University of Technology, Onsala Space Observatory, SE-43992 Onsala, Sweden
[45] Yale Center for Astronomy & Astrophysics, Yale University, 52 Hillhouse Avenue, New Haven, CT 06511, USA
[46] Department of Physics, University of Illinois, 1110 W. Green Street, Urbana, IL 61801, USA
[47] Fermi National Accelerator Laboratory, MS209, P.O. Box 500, Batavia, IL 60510, USA
[48] Department of Astronomy and Astrophysics, University of Chicago, 5640 S. Ellis Avenue, Chicago, IL 60637, USA
[49] East Asian Observatory, 660 N. A'ohoku Place, Hilo, HI 96720, USA
[50] James Clerk Maxwell Telescope (JCMT), 660 N. A'ohoku Place, Hilo, HI 96720, USA
[51] California Institute of Technology, 1200 E. California Boulevard, Pasadena, CA 91125, USA
[52] Department of Physics, McGill University, 3600 rue University, Montréal, QC H3A 2T8, Canada
[53] Trottier Space Institute at McGill, 3550 rue University, Montréal, QC H3A 2A7, Canada
[54] Department of Astrophysics, Institute for Mathematics, Astrophysics and Particle Physics (IMAPP), Radboud University, P.O. Box 9010, 6500 GL Nijmegen, The Netherlands
[55] Department of Physics and Astronomy, University of Waterloo, 200 University Avenue West, Waterloo, ON N2L 3G1, Canada
[56] Waterloo Centre for Astrophysics, University of Waterloo, Waterloo, ON N2L 3G1, Canada
[57] Department of Astronomy, University of Massachusetts, Amherst, MA 01003, USA
[58] Korea Astronomy and Space Science Institute, Daedeok-daero 776, Yuseong-gu, Daejeon 34055, Republic of Korea
[59] University of Science and Technology, Gajeong-ro 217, Yuseong-gu, Daejeon 34113, Republic of Korea
[60] Kavli Institute for Cosmological Physics, University of Chicago, 5640 S. Ellis Avenue, Chicago, IL 60637, USA
[61] Department of Physics, University of Chicago, 5720 S. Ellis Avenue, Chicago, IL 60637, USA
[62] Enrico Fermi Institute, University of Chicago, 5640 S. Ellis Avenue, Chicago, IL 60637, USA
[63] Princeton Gravity Initiative, Jadwin Hall, Princeton University, Princeton, NJ 08544, USA
[64] Physics Department, Fairfield University, 1073 N. Benson Road, Fairfield, CT 06824, USA
[65] Department of Astronomy, University of Illinois at Urbana-Champaign, 1002 W. Green Street, Urbana, IL 61801, USA
[66] Research Center for Intelligent Computing Platforms, Zhejiang Laboratory, Hangzhou 311100, People's Republic of China
[67] Tsung-Dao Lee Institute, Shanghai Jiao Tong University, Shengrong Road 520, Shanghai, 201210, People's Republic of China
[68] Department of Astronomy and Columbia Astrophysics Laboratory, Columbia University, 550 W. 120th Street, New York, NY 10027, USA
[69] Center for Computational Astrophysics, Flatiron Institute, 162 Fifth Avenue, New York, NY 10010, USA

[70] Wits Centre for Astrophysics, University of the Witwatersrand, 1 Jan Smuts Avenue, Braamfontein, Johannesburg 2050, South Africa
[71] Department of Physics, University of Pretoria, Hatfield, Pretoria 0028, South Africa
[72] Centre for Radio Astronomy Techniques and Technologies, Department of Physics and Electronics, Rhodes University, Makhanda 6140, South Africa
[73] ASTRON, Oude Hoogeveensedijk 4, 7991 PD Dwingeloo, The Netherlands
[74] JILA and Department of Astrophysical and Planetary Sciences, University of Colorado, Boulder, CO 80309, USA
[75] Las Cumbres Observatory, 6740 Cortona Drive, Suite 102, Goleta, CA 93117-5575, USA
[76] Department of Physics, University of California, Santa Barbara, CA 93106-9530, USA
[77] Department of Electrical Engineering and Computer Science, Massachusetts Institute of Technology, 32-D476, 77 Massachusetts Avenue, Cambridge, MA 02142, USA
[78] Google Research, 355 Main Street, Cambridge, MA 02142, USA
[79] Institut für Theoretische Physik und Astrophysik, Universität Würzburg, Emil-Fischer-Str. 31, D-97074 Würzburg, Germany
[80] Department of History of Science, Harvard University, Cambridge, MA 02138, USA
[81] Department of Physics, Harvard University, Cambridge, MA 02138, USA
[82] NCSA, University of Illinois, 1205 W. Clark Street, Urbana, IL 61801, USA
[83] CP3-Origins, University of Southern Denmark, Campusvej 55, DK-5230 Odense M, Denmark
[84] Key Laboratory for Research in Galaxies and Cosmology, Chinese Academy of Sciences, Shanghai 200030, People's Republic of China
[85] Mizusawa VLBI Observatory, National Astronomical Observatory of Japan, 2-12 Hoshigaoka, Mizusawa, Oshu, Iwate 023-0861, Japan
[86] Department of Astronomical Science, The Graduate University for Advanced Studies (SOKENDAI), 2-21-1 Osawa, Mitaka, Tokyo 181-8588, Japan
[87] NOVA Submillimeter Instrumentation Group, Kapteyn Astronomical Institute, University of Groningen, Landleven 12, 9747 AD Groningen, The Netherlands
[88] Department of Astronomy, School of Physics, Peking University, Beijing 100871, People's Republic of China
[89] Department of Astronomy, Graduate School of Science, The University of Tokyo, 7-3-1 Hongo, Bunkyo-ku, Tokyo 113-0033, Japan
[90] The Institute of Statistical Mathematics, 10-3 Midori-cho, Tachikawa, Tokyo 190-8562, Japan
[91] Department of Statistical Science, The Graduate University for Advanced Studies (SOKENDAI), 10-3 Midori-cho, Tachikawa, Tokyo 190-8562, Japan
[92] Kavli Institute for the Physics and Mathematics of the Universe, The University of Tokyo, 5-1-5 Kashiwanoha, Kashiwa 277-8583, Japan
[93] Leiden Observatory, Leiden University, Postbus 2300, 9513 RA Leiden, The Netherlands
[94] ASTRAVEO LLC, P.O. Box 1668, Gloucester, MA 01931, USA
[95] Applied Materials Inc., 35 Dory Road, Gloucester, MA 01930, USA
[96] Institute for Astrophysical Research, Boston University, 725 Commonwealth Avenue, Boston, MA 02215, USA
[97] Institute for Cosmic Ray Research, The University of Tokyo, 5-1-5 Kashiwanoha, Kashiwa, Chiba 277-8582, Japan
[98] Joint Institute for VLBI ERIC (JIVE), Oude Hoogeveensedijk 4, 7991 PD Dwingeloo, The Netherlands
[99] Department of Astronomy and Atmospheric Sciences, Kyungpook National University, Daegu 702-701, Republic of Korea
[100] Kogakuin University of Technology & Engineering, Academic Support Center, 2665-1 Nakano, Hachioji, Tokyo 192-0015, Japan
[101] Niigata University, 8050 Ikarashi-nino-cho, Nishi-ku, Niigata 950-2181, Japan
[102] Physics Department, National Sun Yat-Sen University, No. 70, Lien-Hai Road, Kaosiung City 80424, Taiwan, R.O.C.
[103] National Optical Astronomy Observatory, 950 N. Cherry Avenue, Tucson, AZ 85719, USA
[104] Department of Physics, The Chinese University of Hong Kong, Shatin, N.T., Hong Kong
[105] School of Astronomy and Space Science, Nanjing University, Nanjing 210023, People's Republic of China
[106] Key Laboratory of Modern Astronomy and Astrophysics, Nanjing University, Nanjing 210023, People's Republic of China
[107] INAF-Istituto di Radioastronomia, Via P. Gobetti 101, I-40129 Bologna, Italy
[108] Department of Physics, National Taiwan University, No.1, Sec. 4, Roosevelt Road, Taipei 10617, Taiwan, R.O.C
[109] Instituto de Radioastronomía y Astrofísica, Universidad Nacional Autónoma de México, Morelia 58089, México
[110] Instituto de Astronomía, Universidad Nacional Autónoma de México (UNAM), Apdo Postal 70-264, Ciudad de México, México
[111] Yunnan Observatories, Chinese Academy of Sciences, 650011 Kunming, Yunnan Province, People's Republic of China
[112] Center for Astronomical Mega-Science, Chinese Academy of Sciences, 20A Datun Road, Chaoyang District, Beijing 100012, People's Republic of China
[113] Key Laboratory for the Structure and Evolution of Celestial Objects, Chinese Academy of Sciences, 650011 Kunming, People's Republic of China
[114] Anton Pannekoek Institute for Astronomy, University of Amsterdam, Science Park 904, 1098 XH Amsterdam, The Netherlands
[115] Gravitation and Astroparticle Physics Amsterdam (GRAPPA) Institute, University of Amsterdam, Science Park 904, 1098 XH Amsterdam, The Netherlands
[116] School of Natural Sciences, Institute for Advanced Study, 1 Einstein Drive, Princeton, NJ 08540, USA
[117] Science Support Office, Directorate of Science, European Space Research and Technology Centre (ESA/ESTEC), Keplerlaan 1, 2201 AZ Noordwijk, The Netherlands
[118] School of Physics and Astronomy, Shanghai Jiao Tong University, 800 Dongchuan Road, Shanghai 200240, People's Republic of China
[119] Astronomy Department, Universidad de Concepción, Casilla 160-C, Concepción, Chile
[120] National Institute of Technology, Hachinohe College, 16-1 Uwanotai, Tamonoki, Hachinohe City, Aomori 039-1192, Japan
[121] Research Center for Astronomy, Academy of Athens, Soranou Efessiou 4, 115 27, Athens, Greece
[122] Department of Physics, Villanova University, 800 Lancaster Avenue, Villanova, PA 19085, USA
[123] Physics Department, Washington University CB 1105, St Louis, MO 63130, USA
[124] Sejong University, 209 Neungdong-ro, Gwangjin-gu, Seoul, Republic of Korea
[125] School of Physics, Georgia Institute of Technology, 837 State Street NW, Atlanta, GA 30332, USA
[126] Radio Astronomy Laboratory, University of California, Berkeley, CA 94720, USA
[127] Institute of Astrophysics, Foundation for Research and Technology—Hellas, Voutes, 7110 Heraklion, Greece
[128] Department of Physics, National Taiwan Normal University, No. 88, Sec. 4, Tingzhou Road, Taipei 116, Taiwan, R.O.C.
[129] Center of Astronomy and Gravitation, National Taiwan Normal University, No. 88, Sec. 4, Tingzhou Road, Taipei 116, Taiwan, R.O.C.
[130] Finnish Centre for Astronomy with ESO, FI-20014 University of Turku, Finland
[131] Aalto University Metsähovi Radio Observatory, Metsähovintie 114, FI-02540 Kylmälä, Finland
[132] Gemini Observatory/NSF NOIRLab, 670 N. A'ohōkū Place, Hilo, HI 96720, USA
[133] Frankfurt Institute for Advanced Studies, Ruth-Moufang-Strasse 1, D-60438 Frankfurt, Germany
[134] School of Mathematics, Trinity College, Dublin 2, Ireland
[135] Department of Astrophysical Sciences, Peyton Hall, Princeton University, Princeton, NJ 08544, USA
[136] Department of Physics, Tokyo Institute of Technology, 2-12-1 Ookayama, Meguro-ku, Tokyo 152-8551, Japan
[137] Hiroshima Astrophysical Science Center, Hiroshima University, 1-3-1 Kagamiyama, Higashi-Hiroshima, Hiroshima 739-8526, Japan
[138] Aalto University Department of Electronics and Nanoengineering, PL 15500, FI-00076 Aalto, Finland
[139] Department of Astronomy, Yonsei University, Yonsei-ro 50, Seodaemun-gu, 03722 Seoul, Republic of Korea
[140] Department of Physics and Astronomy, University of Lethbridge, Lethbridge, Alberta T1K 3M4, Canada
[141] Netherlands Organisation for Scientific Research (NWO), Postbus 93138, 2509 AC Den Haag, The Netherlands
[142] Department of Physics and Astronomy, Seoul National University, Gwanak-gu, Seoul 08826, Republic of Korea
[143] University of New Mexico, Department of Physics and Astronomy, Albuquerque, NM 87131, USA

[144] Jeremiah Horrocks Institute, University of Central Lancashire, Preston PR1 2HE, UK
[145] Physics Department, Brandeis University, 415 South Street, Waltham, MA 02453, USA
[146] Tuorla Observatory, Department of Physics and Astronomy, University of Turku, Finland
[147] Radboud Excellence Fellow of Radboud University, Nijmegen, The Netherlands
[148] Princeton Gravity Initiative, Princeton University, Princeton, NJ 08544, USA
[149] School of Physics, Huazhong University of Science and Technology, Wuhan, Hubei 430074, People's Republic of China
[150] Mullard Space Science Laboratory, University College London, Holmbury St. Mary, Dorking, Surrey RH5 6NT, UK
[151] School of Astronomy and Space Sciences, University of Chinese Academy of Sciences, No. 19A Yuquan Road, Beijing 100049, People's Republic of China
[152] Astronomy Department, University of Science and Technology of China, Hefei 230026, People's Republic of China
[153] Bard College, 30 Campus Road, Annandale-on-Hudson, NY 12504, USA
Received 2023 May 9; revised 2023 August 28; accepted 2023 August 28; published 2023 November 29

Abstract

In 2017 the Event Horizon Telescope (EHT) observed the supermassive black hole at the center of the Milky Way, Sagittarius A* (Sgr A*), at a frequency of 228.1 GHz ($\lambda = 1.3$ mm). The fundamental physics tests that even a single pulsar orbiting Sgr A* would enable motivate searching for pulsars in EHT data sets. The high observing frequency means that pulsars—which typically exhibit steep emission spectra—are expected to be very faint. However, it also negates pulse scattering, an effect that could hinder pulsar detections in the Galactic center. Additionally, magnetars or a secondary inverse Compton emission could be stronger at millimeter wavelengths than at lower frequencies. We present a search for pulsars close to Sgr A* using the data from the three most sensitive stations in the EHT 2017 campaign: the Atacama Large Millimeter/submillimeter Array, the Large Millimeter Telescope, and the IRAM 30 m Telescope. We apply three detection methods based on Fourier-domain analysis, the fast folding algorithm, and single-pulse searches targeting both pulsars and burst-like transient emission. We use the simultaneity of the observations to confirm potential candidates. No new pulsars or significant bursts were found. Being the first pulsar search ever carried out at such high radio frequencies, we detail our analysis methods and give a detailed estimation of the sensitivity of the search. We conclude that the EHT 2017 observations are only sensitive to a small fraction ($\lesssim$2.2%) of the pulsars that may exist close to Sgr A*, motivating further searches for fainter pulsars in the region.

Unified Astronomy Thesaurus concepts: Radio pulsars (1353); Pulsars (1306); Magnetars (992); Neutron stars (1108); Black hole physics (159); Period search (1955); Surveys (1671); Interstellar scattering (854); Galactic center (565); Supermassive black holes (1663); Radio transient sources (2008); Millimeter astronomy (1061)

1. Introduction

The first test of strong-field gravity came from measurements of the relativistic orbital decay in a binary pulsar system (Taylor & Weisberg 1982, 1989), with subsequent tests of increasing precision using other binary (or even triple) pulsar systems (see, e.g., Wex & Kramer 2020, for a review). So far, all gravity experiments using pulsars conform with the predictions of general relativity (GR), but it is expected that the most constraining tests will come from a pulsar black hole binary system (Wex & Kopeikin 1999; Liu et al. 2014), and in particular from pulsars orbiting Sagittarius A* (Sgr A*) itself (Kramer et al. 2004; Liu et al. 2012). Discovery and timing observations of pulsars near Sgr A* could provide measurements of the spin and quadrupole moment of the supermassive black hole (SMBH), in addition to unique information on Galactic center (GC) stellar populations, dark matter, and the γ-ray excess (Ajello et al. 2016; Bartels et al. 2016; Daylan et al. 2016), along with measurements of the magnetoionic plasma (Eatough et al. 2013; Desvignes et al. 2018).

Together with the groundbreaking measurements of binary black hole mergers with gravitational wave detectors (Abbott et al. 2016) and high-precision astrometry of stars orbiting Sgr A* (Gravity Collaboration et al. 2018, 2019, 2020; Do et al. 2019), millimeter interferometric imaging of SMBHs by the Event Horizon Telescope (EHT) Collaboration represents a transformation in the way black holes can be observed and studied (see Event Horizon Telescope Collaboration et al. 2019a, 2022a, and references therein for an overview of key results). Comparison of EHT image properties with synthetic images derived from general relativistic magnetohydrodynamic simulations, and general relativistic ray tracing, provide a new framework in which to measure the fundamental properties of black holes and test theories of gravity in the strong-field regime (e.g., Mizuno et al. 2018; Event Horizon Telescope Collaboration et al. 2019b, 2019c, 2022b; Özel et al. 2022; Younsi et al. 2023).

EHT images of the SMBHs Messier 87* (M87*) and Sgr A* are consistent with predictions for the black hole shadow of a spinning Kerr black hole in GR, while certain alternative theories of gravity, which deviate from the Kerr metric in the strong-field regime, have been ruled out (Psaltis et al. 2020). For Sgr A*, the EHT images can be synergized with the measurements from an orbiting pulsar. For example, Psaltis et al. (2016) showed that the spin and quadrupole moment of Sgr A* from the motion of orbiting stars (e.g., Weinberg et al. 2005) and pulsars have correlated uncertainties that are almost orthogonal to those from black hole shadow images, thereby increasing overall measurement accuracy.

While estimates of the GC pulsar population range from about a few to several thousand (e.g., Pfahl & Loeb 2004; Wharton et al. 2012; Dexter & O'Leary 2014; Rajwade et al. 2017; Schödel et al. 2020; Chen et al. 2023), only six radio pulsars have been detected within 50 pc (projected) from Sgr A* (Johnston et al. 2006; Deneva et al. 2009), at centimeter

[154] NASA Hubble Fellowship Program, Einstein Fellow.

wavelengths, including the radio magnetar PSR J1745−2900 that lies just 3″ (i.e., a projected distance of 0.1 pc) away (Eatough et al. 2013; Kennea et al. 2013; Rea et al. 2013). Although more sensitive pulsar searches of the GC region have been conducted (e.g., Macquart et al. 2010; Eatough et al. 2021; Suresh et al. 2022), they failed to discover additional pulsars, potentially highlighting the limits of surveys at centimeter wavelengths.

Multipath propagation by scattering from electron-density inhomogeneities typically broadens radio pulse emission, reducing the signal-to-noise ratio (S/N) of periodic or single-burst radio signals (Cordes & Lazio 1997). The severity of this effect depends on the observing frequency ν, ($\sim\nu^n$; where $n \approx -4$), spin period (P), pulse or burst width, and also on the scattering environment toward the GC. The NE2001 model of the Galactic distribution of free electrons (Cordes & Lazio 2002) predicts a large scattering timescale that is inconsistent with the combined measurements of PSR J1745−2900 and Sgr A* (Bower et al. 2014, 2015; Spitler et al. 2014) but may apply to other lines of sight toward ($\lesssim 0.^\circ 5$) the GC (Dexter et al. 2017). Therefore, one rationale is to search the GC at millimeter and submillimeter wavelengths where multipath scattering can be avoided altogether. However, given the average steep spectrum of pulsars' radio emission where flux density $\sim\nu^\alpha$, with α typically between −1 and −2.5 (see, e.g., Jankowski et al. 2018), many pulsars are expected to be faint at frequencies where scattering is negligible. Nevertheless, a subset of pulsars and their high-magnetic-field counterparts, magnetars, show flat or inverted spectra[155] with detectable millimeter and submillimeter emission (Camilo et al. 2007; Torne et al. 2020, 2022; Chu et al. 2021), including from PSR J1745−2900 itself (Torne et al. 2015, 2017).

Additional physical processes may contribute to emission in these bands and could enhance the probability of detection. For example, induced inverse Compton scattering of low-frequency radio photons at frequency ν can produce higher-frequency photons at $\nu' \sim \gamma^2\nu$ in some pulsar models (e.g., Blandford & Scharlemann 1976; Philippov & Kramer 2022), where γ is the Lorentz factor. For example, with $\nu = 100$ MHz and $\gamma = 50$, scattered photons will boost emission at $\nu \sim 250$ GHz. Since a wide range of Lorentz factors is possible, it is necessary to search in a corresponding wide range of observing bands with sensitive millimeter and submillimeter telescopes.

The first attempts at searching the GC for pulsars at millimeter wavelengths were undertaken with the IRAM 30 m Telescope ($\lambda \simeq 2$, 3 mm; Torne et al. 2021) and the Atacama Large Millimeter/submillimeter Array (ALMA; $\lambda \simeq 3.5$ mm; Liu et al. 2021). In this work we report the first 1.3 mm searches for GC pulsars using data from the EHT 2017 campaign on Sgr A*. As well as utilizing the most sensitive millimeter/submillimeter telescopes, the simultaneous EHT observations from multiple telescope sites enable efficient rejection of false-positive detections.

In Section 2 we describe the observations and data processing; in Section 3 the results of our pulsar search of the EHT data are detailed; Section 4 is a discussion of the findings; Section 5 presents potential improvements for the future, and Section 6 summarizes our conclusions.

[155] Around 13% of known pulsars with a measured spectral index have $\alpha \geqslant -1.0$ (Manchester et al. 2005; PSRCAT in 2023).

2. Observations and Data Processing

2.1. Observations

The EHT 2017 observing campaign was scheduled on five nights during 2017 April 5–14, where three nights (April 6, 7, and 11) included exposures to Sgr A* ($\alpha_{J2000} = 17^h45^m40.^s0361$, $\delta_{J2000} = -29^\circ00'28.''168$). At each epoch, the track on Sgr A* was divided into individual scans of approximately 7−10 minutes each, switching between Sgr A* and an active galactic nucleus calibrator source, J1924−2914 and/or NRAO 530. Baseband voltage data were recorded with 2-bit sampling at a total rate of 32 Gbps in two 2 GHz IF-bands centered at 229.1 and 227.1 GHz, labeled "high" and "low," respectively. More details of the EHT array, the observations, and data recording can be found in Event Horizon Telescope Collaboration et al. (2019d, 2019e, 2022c).

Since system sensitivity is one of the primary considerations for a pulsar search of the GC, we chose to analyze data only from the three most sensitive telescopes in the EHT 2017 observations: the phased ALMA, the Large Millimeter Telescope Alfonso Serrano (LMT), and the IRAM 30 m Telescope (PV). While the sensitivity of phased ALMA is significantly higher than the other two stations, its field of view, given by the FWHM of its synthetic beam during the EHT 2017 observations on Sgr A*, is only 1″–2″ (Goddi et al. 2021); offering comparatively limited sky coverage. LMT and IRAM 30 m, both of which are used here as single-dish telescopes with a beam size of approximately 10″ at 1.3 mm, are useful in supplementing the sky coverage of ALMA for the pulsar search (see Section 4.3 for more details) and covering the position of PSR J1745−2900. The total length of the tracks on Sgr A* of these telescopes varied from 5–10 hr on different nights, and are summarized in Table 1.

2.2. Data Conversion and Preparation

The baseband voltage data were captured by Mark 6 recorders[156] at the telescopes, and the disk packs shipped to the correlator at the Max Planck Institute for Radio Astronomy in Bonn, Germany, for post-processing. The voltage data selected for the pulsar search were reduced into multichannel intensity time series (commonly referred to as a *filterbank*) written in search-mode PSRFITS format, a standard FITS specification for pulsar data (Hotan et al. 2004).[157] This used the software tool `MPIvdif2psrfits`,[158] an upgraded version of the original toolkit developed under the ALMA Pulsar Mode Project[159] (Liu et al. 2019) that incorporates parallel processing capability using `OpenMPI`.[160] The resulting properties of the PSRFITS products are presented in Table 1.

After conversion to PSRFITS, the data consisted of a number of short scans for each of the two frequency sub-bands (high and low), corresponding to observations of Sgr A*, a calibrator, or another science target. From the scans on Sgr A*, those showing potential issues were flagged to be excluded from the analysis. The main reasons to flag scans were large variations

[156] https://www.haystack.mit.edu/mark-6-vlbi-data-system/
[157] https://www.atnf.csiro.au/research/pulsar/psrfits_definition/PsrfitsDocumentation.html
[158] https://github.com/xuanyuanstar/MPIvdif2psrfits
[159] http://hosting.astro.cornell.edu/research/almapsr/
[160] https://www.open-mpi.org/

Table 1
Details of Observations and Data Analyzed in This Paper

Station	D_S (m)	FWHM (arcsec)	ν_{obs} (GHz)	$\Delta\nu$ (GHz)	n_{ch}[b]	t_{samp}[b] (μs)	Total Time Span (hr)			Net Time on Sgr A* (hr)		
							Apr 6	Apr 7	Apr 11	Apr 6	Apr 7	Apr 11
ALMA	74	1−2	228.1	3.75[c]	64	8	4.6	10.2	3.6	2.1	4.6	1.9
LMT	50 (32.5[a])	10	228.1	4.00	32	8	5.7	6.4	3.6	2.4	3.0	1.7
IRAM 30 m	30	10.8	228.1	4.00	32	8	⋯	3.2	⋯	⋯	1.1	⋯

Notes. The first seven columns indicate the EHT station, the real (or equivalent for the phased ALMA array) single-dish diameter (D_s), the effective beam FWHM, the central observing frequency (ν_{obs}), the total effective bandwidth ($\Delta\nu$), the number of frequency channels (n_{ch}), and the initial sample time (t_{samp}), in the resulting PSRFITS files[b]. The remaining columns show, for each epoch, the total time span of the data set constructed for the pulsar search (i.e., the time between the start of the first scan and the end of the last scan) and the net integration time on Sgr A*. The difference between the total time span and the net integration time is due to the interleaved observations of calibrators, slew time of the telescope, time for pointing and focus adjustments, and the flagged data. The data with the total time span are the ones searched, but only the net integration time on Sgr A* is considered for the search sensitivity analysis.
[a] Though the full geometric diameter of LMT is 50 m, during the EHT 2017 campaign, only 32.5 m were illuminated.
[b] During data preparation, the number of frequency channels and sample time was reduced to varying degrees (see Section 2.2).
[c] Due to slightly overlapping channels in the digital filterbank, the effective bandwidth is 2 × 1.875 GHz (see Goddi et al. 2019).

or jumps of the mean power level, and, specifically for the case of ALMA, those scans not showing the expected array phasing noise features (see Section 2.2.1).

Once the selection of Sgr A* scans to be analyzed were identified for ALMA, LMT, and IRAM 30 m, the data were further prepared for pulsar searching. The steps for each telescope are presented in the following subsections.

2.2.1. Atacama Large Millimeter/submillimeter Array

When ALMA is used as a phased array, the scans are partitioned into subscans with updates of the phase corrections every 18.192 s to enable the coherent summation of signals from individual antennas (Goddi et al. 2019). This phasing cycle introduced a periodic feature in the time series, consisting of a decrease in the power level with a duration slightly below 2 s, followed by a large negative peak (we hereafter refer to this feature as the "broad" feature). Additionally, a forest of negative narrow spikes occurred a few seconds after the broad feature (see the Appendix of Liu et al. 2021, for details). The first step in the preparation of the ALMA data was therefore to try to remove those noise features, which could introduce undesired power in the Fourier domain and decrease the sensitivity to pulsars in the search. To locate and clean the features, we first produced a time series collapsing all of the frequency channels of the PSRFITS file with the routine `prepdata` of the software package PRESTO (Ransom 2011),[161] downsampling the time resolution to 32 μs, and visually inspected each scan, marking the center of the first appearance of the broad feature. Then, 2 s wide windows around the first broad feature position, and every 18.192 s thereafter, were replaced with the mean level of the time series calculated outside the marked windows. Next, we use a moving window of width 10 s that clips negative narrow spikes below a threshold of five times the standard deviation of the samples within the window. The flagged data due to the phasing features correspond to ≈11% of the total.

Before combining the two frequency sub-bands (low and high) to obtain a full-bandwidth data set, we remove slow variations of the mean power level in the time series with a "running-fit" filter that fits and subtracts a first-order polynomial in a running window of 10 s. This step reduces the excess of power in the low-frequency end of the Fourier-domain data (also known as "red noise"), which tend to be large in millimeter observations due to atmospheric opacity variations during observations. We also normalize the time series by its standard deviation to combine the low and high sub-bands with a similar rms level. At this stage, the cleaned time series of each individual scan and sub-band is saved as a SIGPROC[162]-format filterbank file (Lorimer 2011) with one single frequency channel of 2 GHz and a time sampling of 32 μs, except for April 7, where we downsample to 64 μs to reduce the data size and speed up the processing of this particularly long epoch. The production of the SIGPROC filterbank files is made with custom Python code supported by tools from PRESTO and SIGPYPROC.[163]

Then, for each sub-band, we concatenate all of the scans for each observing track into a single, continuous SIGPROC filterbank file, padding the gaps in between scans with the mean value. This concatenation is necessary to maintain the coherence of the data and maximize the sensitivity to periodic signals like those expected from pulsars. Before the next step, we ensure that the start time and length are equal between the concatenated files in the low- and high-band data sets, adjusting the length if necessary. Finally, we splice together the two frequency sub-bands into one file with the `splice` routine of SIGPROC. The result is a two-channel filterbank file containing all of the scans of the observing track with the full bandwidth. This process is repeated for each night, and the final filterbank files are those passed to the searching pipelines (see Section 2.3).

In a separate step, we Fourier transformed and analyzed with PRESTO's `accelsearch` routine three scans on calibrators (one for each observing night) to obtain a list of locally generated periodic signals through an analysis of the corresponding Fourier spectrum. A list of periodicities—most likely produced in the receiving chain—is created, and later used to flag them when applying the searching pipeline to the observations on Sgr A* by zero-weighting the corresponding Fourier bins.

[161] https://github.com/scottransom/presto
[162] https://sigproc.sourceforge.net
[163] https://github.com/ewanbarr/sigpyproc

2.2.2. IRAM 30 m Telescope

The IRAM 30 m Telescope data were mainly affected by two features: a strong ripple in the time series with a frequency of about 210.7 Hz, and regular power drop-offs, part of them synchronized with the 210.7 Hz cycle (see Figures 6 and 7 in the Appendix). The origin of these noise features is under investigation, suspected to be related to oscillations in the bias circuits of the first mixer of the receiver. To reduce the impact in the subsequent analysis, we first zero-weight a few Fourier bins centered on the 210.7 Hz signal, including three harmonics. We also zero-weight a few bins around 1 Hz, to remove another strong periodic signal related to the cryogenic pump cycle. To reduce the number of power drop-offs, we visually inspected the resulting time series, and manually marked a threshold below which all samples were substituted with the median of the remaining data. The percentage of data flagged related to the power drop-offs was on average 2.8%. The following steps are analogous as for the ALMA data: a running-fit filter with a window of 10 s to subtract slow mean level variations, a normalization of the data by their standard deviation, and a concatenation of scans plus splicing into a single filterbank file. Five scans showing larger instabilities in the form of ripples or considerably more signal drop-offs than on average, amounting to 0.72 hr in total, were flagged and excluded from the analysis.

2.2.3. Large Millimeter Telescope

The data from the LMT show strong periodicities associated with the local receiver. The most prominent signals have a frequency of 1.2 Hz, probably related to the cryogenics refrigeration cycle, and around 185 Hz, which has an unknown origin. The data also show some power drop-offs, but less frequently than the ALMA and IRAM 30 m data. A variation of the mean power level is usually present, related to opacity variations during the observations (see Figures 6 and 7 in the Appendix). To reduce these undesired signals, we zero-weight the strongest peaks related to the 1.2 and 185 Hz signals in the Fourier domain, and after an inverse Fourier transform, use a moving window of 10 s that clips the power-drops substituting them with the median value inside the window. The mean power level variations are minimized using the running-fit filter with a window of 10 s, as done for the ALMA and IRAM 30 m data. The remaining steps—normalization, concatenation, and splicing—are analogous to the ALMA and IRAM 30 m data sets. For the LMT, 16 scans in total (amounting to 2.32 hr) were flagged because they still showed clear artifacts after the cleaning, like jumps in the mean power level and regular trains of strong, wide-pulse-like features.

We remark that although the undesired signals are highly reduced in the data from the three stations by our cleaning algorithms, they are not fully removed. We show examples of the time series before and after the cleaning procedures in the Appendix.

2.3. Pulsar Searching

Searching for pulsars via their inherent periodicity is done with two independent pipelines: a Fourier-domain search (Ransom et al. 2002) and a search using the fast folding algorithm (FFA; Staelin 1969). Fourier-domain methods are widely used in pulsar searches and have proven successful in discovering pulsars with a variety of spin parameters (Lyne 2003). The FFA works particularly well at detecting long-period pulsars that often show narrow pulse profiles (Cameron et al. 2017; Morello et al. 2020). In addition, we searched the data for single-pulse burst-like transient emission[164] as seen in pulsar giant pulses, rotating radio transients, and fast radio bursts (see, e.g., Keane et al. 2011). In the following subsections, we detail the search algorithms used. The parameters utilized for each pipeline are summarized in Tables 2 and 3.

Pulsar surveys at low radio frequencies typically search over a range of dispersion measures (DMs)—the integrated column density of free electrons along the line of sight. However, there is no de-dispersion in our pipelines because the effect of even large DMs is negligible at the EHT observing frequencies and for the target time resolution of 32 μs. Interstellar dispersion delays the pulses' arrival times scaling with DM ν^{-2} (see, e.g., Lorimer & Kramer 2004), but a DM = 10,000 pc cm^{-3} would produce a pulse smearing of only $\Delta t_{\rm DM} \simeq 28\ \mu$s across our $\sim$4 GHz band. The highest DM known to date is for the magnetar PSR J1745−2900, located close to Sgr A*, at DM = 1778 pc cm^{-3} (Eatough et al. 2013). The negligible dispersion has some disadvantages (see Sections 2.3.3, 5.3), but reduces considerably the computing costs, which can be concentrated on the acceleration search.

2.3.1. Periodicity Search in the Fourier Domain

The Fourier-domain pipeline predominantly searches for pulsars by detecting and analyzing peaks in the Fourier spectrum of the time series. We use the software PRESTO, which includes the capability to search for accelerated pulsars, like those orbiting Sgr A* or other companions. The acceleration parameter space is searched using a template-matching algorithm by recovering the power spread over contiguous Fourier bins (Ransom et al. 2002). This power spread is the result of the Doppler effect when a pulsar changes its radial velocity during an observation.

A limitation of the template-matching algorithm is that it loses efficiency for observations covering a substantial fraction of the binary period ($P_{\rm b}$). This limiting fraction is about $0.1P_{\rm b}$ (given a companion mass of 1.4 solar mass), i.e., the algorithm works well when the total observing time does not exceed ~10% of the binary period (e.g., Ransom 2001; Ng et al. 2015). To improve the sensitivity for longer observing spans, one can add a search in the line-of-sight acceleration derivative (commonly referred to as "jerk") parameter space (Andersen & Ransom 2018), although this greatly increases the computational costs.[165] The line-of-sight acceleration ($a_{\rm l}$) and its derivative ($j_{\rm l}$) of a pulsar in orbit can be calculated as (e.g., Bagchi et al. 2013):

$$a_{\rm l} = -\left(\frac{2\pi}{P_{\rm b}}\right)^2 \frac{a_{\rm p} \sin i}{(1-e^2)^2} \sin(A_{\rm T} + \omega)(1 + e\cos A_{\rm T})^2\,, \quad (1)$$

[164] See Mus et al. (2022), who carried out a search for transients with the ALMA data but at longer (∼seconds to minutes) timescales and therefore not sensitive to the same emission sources.

[165] The number of computations scales roughly proportionally to the square of the total observing time for searching acceleration, and with the cube when adding a jerk search.

Table 2
Summary of the Parameters of the Two Periodicity-search Pipelines

Station	Epoch	Pipeline	Parameters									$N_{\rm cands}$
			zmax	wmax	N_h	$\sigma_{\rm sift}$	$P_{\rm min}$ (s)	$P_{\rm max}$ (s)	$a_{\rm l}$ (m s^{-2})	$N_{\rm bin}$	S/N$_{\rm FFA}$	
ALMA	2017 Apr 6	FFT$_1$	1200	0	32	>2.0	…	…	…	…	…	539
		FFT$_2$	300	900	32	>2.0	…	…	…	…	…	1043
		FFA$_1$	…	…	…	…	1	1025	0	512	⩾6.0	16
		FFA$_2$	…	…	…	…	1	1025	±50	128	⩾6.0	556
	2017 Apr 7	FFT$_1$	1200	0	32	>2.0	…	…	…	…	…	175
		FFT$_2$	300	900	32	>2.0	…	…	…	…	…	341
		FFA$_1$	…	…	…	…	1	1025	0	512	⩾6.0	37
		FFA$_2$	…	…	…	…	1	1025	±50	128	⩾6.0	1725
	2017 Apr 11	FFT$_1$	1200	0	32	>2.0	…	…	…	…	…	315
		FFT$_2$	300	900	32	>2.0	…	…	…	…	…	733
		FFA$_1$	…	…	…	…	1	1025	0	512	⩾6.0	91
		FFA$_2$	…	…	…	…	1	1025	±50	128	⩾6.0	619
LMT	2017 Apr 6	FFT$_1$	1200	0	32	>2.0	…	…	…	…	…	162
		FFT$_2$	300	900	32	>2.0	…	…	…	…	…	262
		FFA$_1$	…	…	…	…	1	1025	0	512	⩾6.0	43
		FFA$_2$	…	…	…	…	1	1025	±50	128	⩾6.0	512
	2017 Apr 7	FFT$_1$	1200	0	32	>2.0	…	…	…	…	…	67
		FFT$_2$	300	900	32	>2.0	…	…	…	…	…	92
		FFA$_1$	…	…	…	…	1	1025	0	512	⩾6.0	10
		FFA$_2$	…	…	…	…	1	1025	±50	128	⩾6.0	26
	2017 Apr 11	FFT$_1$	1200	0	32	>2.0	…	…	…	…	…	139
		FFT$_2$	300	900	32	>2.0	…	…	…	…	…	262
		FFA$_1$	…	…	…	…	1	1025	0	512	⩾6.0	50
		FFA$_2$	…	…	…	…	1	1025	±50	128	⩾6.0	145
IRAM 30 m	2017 Apr 11	FFT$_1$	1200	0	32	>2.0	…	…	…	…	…	33
		FFT$_2$	300	900	32	>2.0	…	…	…	…	…	66
		FFA$_1$	…	…	…	…	1	1025	0	512	⩾6.0	454
		FFA$_2$	…	…	…	…	1	1025	±50	128	⩾7.0	4179

Notes. Columns show the station, epoch, pipeline (with subscript indicating different passes with different parameters), parameters used in each case (see Sections 2.3.1 and 2.3.2 for details), and number of pulsar candidates produced in each search pass. A "…" symbol indicates that for that pipeline the parameter is not applicable.

and

$$j_{\rm l} = -\left(\frac{2\pi}{P_{\rm b}}\right)^3 \frac{a_{\rm p}\sin i}{(1-e^2)^{7/2}}(1+e\cos A_{\rm T})^3 \cdot [\cos(A_{\rm T}+\omega) + e\cos\omega - 3e\sin(A_{\rm T}+\omega)\sin A_{\rm T}], \quad (2)$$

where $a_{\rm p}$, i, e, ω, and $A_{\rm T}$ are the semimajor axis, inclination angle, eccentricity, longitude of periastron, and true anomaly of the orbit, respectively.

Our PRESTO-based pipeline is based on that used by Torne et al. (2021). It first produces a time series from the filterbank file and then uses a fast Fourier transform (FFT) to transform the data to the frequency domain. Next, it searches for periodic signals as discussed above. To increase the sensitivity to long-period pulsars, the `rednoise` filtering routine of PRESTO is applied to further decrease the red noise. Up to $N_h = 32$ harmonics of each detected periodicity are summed.

To be sensitive to a wide range of different pulsar systems, two passes on each observation are made. In the first pass, highly accelerated pulsars are searched, and a second pass searches for accelerated pulsars including a search in the jerk parameter space. In both cases, searches for isolated pulsars (i.e., with no acceleration) are included. The control of the ranges for surveying acceleration and jerk are made through the parameters `zmax` = max(|z|) and `wmax` = max(|w|) of the routine `accelsearch`, which in turn represent the maximum shift in the Fourier frequency bin (z) and its derivative (w) within an entire observation of length $T_{\rm obs}$ that the pipeline will search. Following Andersen & Ransom (2018), these two terms can be written as:

$$z = \frac{a_{\rm l} h f T_{\rm obs}^2}{c}, \quad (3)$$

Table 3
Parameters and Results of the Search for Single Pulses and Transients

Data Set	$\sigma'_{\rm SP}$	$N^{\rm SP}_{\rm cand}$	$S^{\rm 1\,ms}_{\rm min}$ (Jy)	$S^{\rm 10\,ms}_{\rm min}$ (Jy)	$S^{\rm 50\,ms}_{\rm min}$ (Jy)
Apr 6, ALMA	6	10	0.26	0.08	0.03
Apr 6, LMT	10	574	38.04	12.03	5.38
Apr 7, ALMA	6	1231	0.25	0.08	0.04
Apr 7, LMT	10	1125	27.51	8.70	3.89
Apr 7, IRAM 30 m	10	3822	6.41	2.03	0.91
Apr 11, ALMA	6	68	0.41	0.13	0.06
Apr 11, LMT	10	63	23.01	7.28	3.25

Note. Columns show the data set analyzed (date and station), the signal-to-noise threshold used for single-pulse events ($\sigma'_{\rm SP}$), the number of single pulses detected ($N^{\rm SP}_{\rm cand}$), and flux density limits ($S_{\rm min}$) for single pulses of representative widths 1, 10, and 50 ms.

and

$$w = \frac{j_1 h f T_{\rm obs}^3}{c}, \quad (4)$$

where f, c, and h represent the pulsar rotational frequency, speed of light, and the index of the Fourier harmonic. Here, we use zmax = 1200 and wmax = 0 for the pass aiming for highly accelerated pulsars, and zmax = 300 and wmax = 900 for the pass including a jerk search. For isolated pulsars, both parameters are set to zero.

The exact relationship between sensitivity, pulsar spin period, acceleration (or orbital period), jerk, pipeline parameters, and observing time is complex (see, e.g., Eatough et al. 2021; Liu et al. 2021). Nonetheless, with the parameters zmax and wmax chosen here, we can correct for the line-of-sight acceleration of virtually any pulsar orbiting Sgr A* down to orbital periods $P_{\rm b} \geqslant 2.5$ yr (assuming circular orbits). Pulsars in orbits with shorter orbital periods can still be detected, depending on their strength and spin period. A more detailed discussion on the coverage of pulsar orbits by our search is presented in Section 4.3.

After all of the pulsar candidates found by accelsearch are saved, a sifting step removes duplicated and harmonically related ones. This step admits pulsar candidates with $\sigma_{\rm sift} \geqslant 2.0$ as calculated by the sifting.py code.[166] Such a $\sigma_{\rm sift}$ threshold allows for the detection of weak pulsars while maintaining a manageable number of candidates (see Torne et al. 2021, and Section 2.4). A final step uses prepfold to fold[167] the data with the information of each candidate, producing plots that can be inspected to decide if any of the candidates corresponds to a real pulsar.

The folding step produces four plots from each candidate. Two of these plots correspond to the raw data with and without an optimization of candidate parameters from prepfold. The other two plots arise from a filtered version of the raw data using the rednoise filter from PRESTO. The rednoise filter is very effective in reducing some local, interfering periodic signals in some data sets, and can in some cases be key to enabling a detection (for an example, see Figure 2 in Torne et al. 2021). This multiple candidate plot production, in exchange of increasing the number of candidate plots to inspect, decreases the risk of missing weak pulsars by an insufficient cleaning or by interference from the locally generated periodic signals.

2.3.2. Periodicity Search with Fast Folding Algorithm

Unlike the Fourier-domain pipeline, the FFA searches for pulsars by folding the time series at different trial periods, forming a sequence of profiles, and testing the significance of each profile using boxcar matched filters. The pulse width and arbitrary total pulse power produced by the filters are used to calculate the signal-to-noise ratio ($S/N_{\rm FFA}$) of the pulse profiles (see, e.g., Cameron et al. 2017, for details). We used the software RIPTIDE[168] (Morello et al. 2020) as the basis for the FFA search pipeline. We include an acceleration search by resampling the time series using SIGPYPROC at a series of acceleration trials using a custom pipeline (Wongphechauxsorn et al. 2024). This implementation of the FFA pipeline assumes a constant acceleration during an observation.

The RIPTIDE software uses a matched filter to detect the pulse in the folded data, making the number of folding profile bins ($N_{\rm bin}$) an important parameter. If the duty cycle is less than one bin, the sensitivity will be reduced. Morello et al. (2020) demonstrated that the number of trials is proportional to $N_{\rm bin}^3$. Folding with many profile bins consequently results in more trials and longer processing times. Furthermore, the acceleration step between trials is proportional to $N_{\rm bin}$; thus, the total number of trials is proportional to $N_{\rm bin}^4$.

Our FFA pipeline uses the cleaned time series generated following the description in Section 2.2. We applied the FFA acceleration search to the time series for periods from $P_{\rm min} = 1$ s to $P_{\rm max} = 1025$ s, using $N_{\rm bin} = 128$. As a result, the pipeline provides full sensitivity to duty cycles down to about 1%).[169] We used an acceleration range of $a_1 = \pm 50\ {\rm m\ s^{-2}}$, i.e., approximately equivalent to zmax = 1400 for detecting a 1 s pulsar in the Fourier domain acceleration search pipeline with $N_h = 32$ and $T_{\rm obs}$ of 4.5 hr. The FFA can therefore probe the same type of binary orbit as the Fourier-domain acceleration search for long-period pulsars. Furthermore, the FFA pipeline is sensitive to an acceleration derivative up to approximately $2.6 \times 10^{-5}\ {\rm m\ s^{-3}}$ without needing any jerk search. The range of acceleration derivative covered is equivalent approximately to a wmax = 10 for a 1 s pulsar in the Fourier domain acceleration search pipeline with the same parameters ($N_h = 32$ and $T_{\rm obs} = 4.5$ hr).

In addition, to search for very narrow duty cycles, the FFA was repeated using $N_{\rm bin} = 512$ with no acceleration, meaning that the pipeline is sensitive to pulsars with a duty cycle larger than 0.19% (only ≈0.2% of currently known pulsars have a lower duty cycle). All candidates detected with $S/N \geqslant 6$ generated by either the accelerated or nonaccelerated pipeline were folded to be inspected visually.

2.3.3. Single-pulse Search

While a pulsar signal is often characterized as a series of stable pulsations, individual single pulses—which can be orders of magnitude brighter than the averaged pulse emission—are observed in some cases (McLaughlin & Cordes 2003) and are detectable with alternative search techniques (Cordes & McLaughlin 2003). For this task, we employed single_pulse_search.py in PRESTO. This routine identifies pulses by matched-filtering the time series with boxcar filters of different pulse widths up to a maximum of 300 samples; corresponding to 9.6 ms and 19.2 ms for our data sets re-sampled at 32 μs and 64 μs, respectively. To avoid excessive automatic time series flagging, we adjusted the

[166] In general, PRESTO's σ values provide a way to estimate if a signal is due to noise or not. While the powers are χ^2 distributed, PRESTO makes a conversion to equivalent Gaussian significance. The parameter $\sigma_{\rm sift}$ therefore indicates the probability of a signal not being produced just by the noise. The code takes into account the number of trials in the search, normalizing to a "single-trial" probability.

[167] Folding is a common technique used in high-time-resolution observations of pulsars in which a long observation is split in blocks of length equal to the spin period of a target pulsar. Then, the blocks are summed or averaged together. The result, in the case of a detection, is an averaged profile of the pulsar emission during the observation, together with a substantial improvement in sensitivity due to an increase of the S/N by the addition of the pulsar signal in each block.

[168] https://github.com/v-morello/riptide

[169] The duty cycle was calculated using the period pulse width from PSRCAT (Manchester et al. 2005). Nota bene, less than 7% of known pulsars have a lower duty cycle.

single_pulse_search.py internal parameters lo_std and hi_std to 0.88 and 3.68, respectively. For the EHT data at 1.3 mm, pulse dispersion is negligible, so it cannot be used as the marker of a genuine astrophysical pulse. Instead, the simultaneous nature of observations conducted at multiple sites is utilized to match coincident pulses from each telescope in the common rest frame of the solar system barycenter.

In practice, single_pulse_search.py gives information on the single-pulse significance, σ_{SP}, its arrival time along with the corresponding number of samples relative to the beginning of the observation and the pulse width (determined by the optimum boxcar filter size). By transforming all of the single-pulse arrival times from each site to their equivalent barycentric Modified Julian Date—determined from PRESTO using the NASA Jet Propulsion Laboratory planetary ephemeris DE405[170] in TEMPO (Nice et al. 2015)[171]—we search for pulses that are coincident to an accuracy of one time sample (32 or 64 μs depending on data set).

In addition, any pulse with $\sigma_{SP} > 12$ is visually inspected (regardless of coincidence) to check for other astrophysical markers such as scatter broadening of the profile or "multi-component profiles," as seen in many pulsars. This also accounts for different Sgr A* visibility windows at each station, their various individual single-pulse sensitivities, and the different spatial coverages due to different beam sizes (see Tables 1 and 3).

2.4. Verification of Periodicity Search Pipelines with Synthetic Signal Injections

Similarly to the method in Torne et al. (2021), before searching the data, a number of pre-processing tests were carried out to verify and tune the pipelines. This was done by injecting synthetic pulsars into the real data and checking their correct detection. The signals were produced with a custom-version of SIGPROC's fake and injected to the filterbank files. The synthetic pulsars included slow-spinning pulsars ($P \geqslant 2$ s), canonical pulsars ($P \sim 500$ ms), and fast-spinning millisecond pulsars (MSPs; 1 ms $< P \leqslant 30$ ms). Within each category, different intensities and duty cycles were used, and both isolated and binary pulsars in a range of configurations were injected. The simulated companions included neutron stars, stellar-mass black holes, and an SMBH with the mass of Sgr A*.

The tests served two main purposes: first, to allow for fine adjustments of the pipeline parameters so that injected signals were recovered, and second, to verify that even extreme pulsar systems, like MSPs in tight orbits around massive companions, were detected when the characteristics were within the theoretical limitations of the searching algorithms (see Section 4.3). Here we confirmed the need for a low value of PRESTO's sifting.py sigma threshold, which is a significance threshold used to accept or reject candidates after a sifting step (set to $\sigma_{sift} > 2.0$), together with a weak requirement on the minimum number of harmonics required per candidate, which is set to one (Torne et al. 2021).

[170] https://ssd.jpl.nasa.gov/planets/eph_export.html
[171] https://tempo.sourceforge.net

3. Results

3.1. Periodicity Search

3.1.1. Fourier-domain Acceleration Search

The analysis with the Fourier-domain pipeline of the three epochs of ALMA resulted in 3146 pulsar candidates. However, no new pulsars were discovered. We identify a large number of candidates with a round number in the spin period or frequency (e.g., $\nu_s = 437.500000$, 111.111111, and 2875.000000 Hz). Another remarkable characteristic of the detected signals is a very short period, with 56.3% of the candidates having $P <$ 0.5 ms. Those characteristics, in particular the round numbers, suggest a human-generated origin. Furthermore, we observe similar signals in the analysis of off-source scans (see Section 2.2.1), and we therefore relate these found periodicities to the local receiving chain and the properties of the Superconductor-Insulator-Superconductor (SIS) receivers used in the observations (see also Torne et al. 2021).

The single epoch with the IRAM 30 m Telescope resulted in 99 pulsar candidates. No signal resembling a real pulsar was found. The candidates are similar in properties to those detected for ALMA, with a significant number showing round values in frequency, and the majority with short periods, with $P \leqslant 4$ ms. The IRAM 30 m Telescope also used an SIS receiver, and similarly to the case of ALMA, we relate the candidates to local oscillations inside the receiver or data transport chains.

Searching the three epochs from the LMT yielded 984 candidates. One candidate stands out after the analysis, with a spin period very close to 32 ms. After a careful examination, we conclude that this candidate is related to locally generated periodic signals or a digitization artifact, because the spin period is almost exactly 1000 times the sampling time of 32 μs. Other reasons to classify this candidate as local are its high power, the fact that the signal suffers at least one significant jump in rotational phase during two of the three observed epochs, and because the same signal is not detected in the ALMA nor the IRAM 30 m data sets. Other strong periodicities at 100, ~180, and 200 Hz are detected in the LMT data, and they are likely related to the power supply. Similarly to the other stations, the data show a significant number of candidates found at round periodicities (both in period or frequency). We conclude that no new pulsars are discovered in the LMT data.

Table 2 provides details of the number of candidates from each epoch, station, and searching pass, and we represent visually the spin period of the candidates in Figure 1.

3.1.2. Fast Folding Algorithm with Acceleration Search

The FFA pipeline applied to the ALMA data resulted in 3044 candidates. The strongest candidate had a period around 18.2 s, which is close to the feature found in the raw ALMA data due to the phasing cycle. The rest of the candidates have a period close to the harmonics of this signal. This candidate and its harmonics likely originate from residual contamination from the known 18.2 s period phasing features.

The FFA pipeline on the LMT data resulted in 300 candidates. Most of the candidates with S/N > 7 showed repetitions of the pulse in the folded profile, indicating that the fundamental periods of these signals are below our period search range. The candidates also have periods with highly round numbers, e.g., 1.0000 s, 2.5000 s, and 1.6000 s. We conclude that these candidates have a local origin.

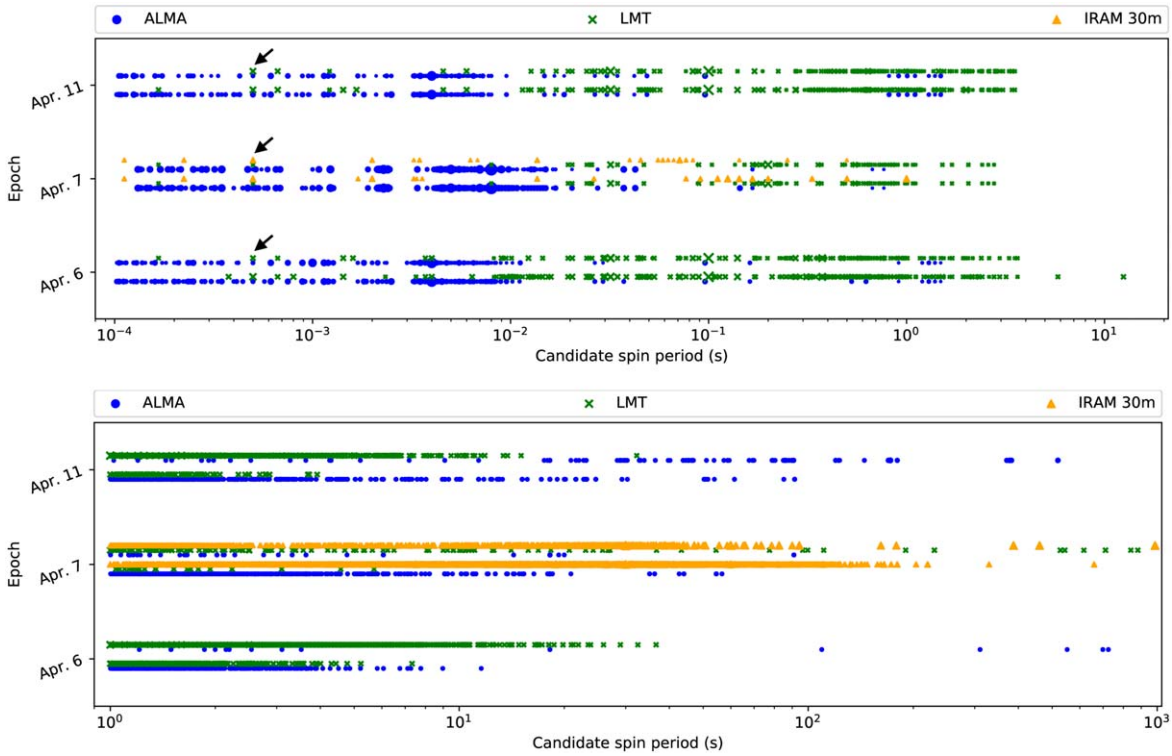

Figure 1. Spin period of the candidates from the two periodicity-search pipelines: Fourier-domain analysis (top panel) and FFA (bottom panel). Each epoch shows two lines of markers, corresponding to the two data processing passes with each pipeline (labeled as FFT_1, FFT_2, FFA_1, and FFA_2 in Table 2). The blue circles, green crosses, and orange squares represent the candidates from ALMA, LMT, and the IRAM 30 m Telescope, respectively. The size of the marker is proportional to the $\sigma_{\rm sift}$, and S/N values, for the Fourier-domain and FFA cases, respectively. None of the candidates are a convincing pulsar signal after the inspection of their candidate evaluation plots. The black arrows in the top panel indicate the $P = 0.5$ ms candidate, the only periodicity present in all data sets and related to a locally generated signal at $\nu = 2000$ Hz (see Section 3.1.3).

For the IRAM 30 m, the FFA search with acceleration yielded over 16,000 candidates. This number is much higher than the number of candidates detected for ALMA and the LMT, indicating that our S/N threshold is likely too low, resulting in too many false candidates. To limit the number of accepted candidates, the minimum S/N was increased to 7, reducing the candidates to 4185 while still maintaining a low significance limit.

A strong candidate at 3.0 s was found without acceleration, with detections of harmonics (i.e., period of 6.000 s and even 150.0 s). This candidate's period is close to an integer to the third decimal, suggesting that it is not astrophysical. We confirmed that this candidate likely originates locally by a repeat of the search in topocentric frame, which yields the same candidate with an exact period of 3.000 s.

We conclude that no pulsars were found by the FFA pipeline. Table 2 includes a summary of the candidates, and Figure 1 is a visual presentation of the candidates' spin periods.

3.1.3. Comparison of Candidates among Stations

Apart from an individual review of all candidates, we cross-checked repetitions of periodicities between epochs and stations. For the Fourier-domain pipeline, we use a similar method as for the single-pulse coincidence matching (see Section 2.3.3) based on `numpy_intersect_1D`. To match candidates with periodicities that may not coincide exactly (this can occur, for example, by a slightly different result of optimization of parameters from `prepfold`), we cross-check the periodicities with precision down to 100 μs. From the 442 reviewed coincidences, none resembles a real pulsar signal; the results are again dominated by local round-number periodicities.

In the few cases where repetitions of periodicities with no round values are found, the characteristics of the candidate (e.g., significance or profile shape) made us classify them as false, produced again likely by local signals or the noise. The most repeated candidate in this step was the $P = 0.5$ ms, identifiable in Figure 1. This $P = 0.5$ ms candidate is clearly detected in the three stations at all epochs. It is however related to a local signal at a frequency of $\nu_s = 2000$ Hz. The fact that it exists in all of the data sets reinforces a relationship with the EHT-specific backend (e.g., its clock signal generator, digitizers, and/or Mark 6 recorders), which were common hardware at the three telescopes. For the FFA pipeline, the periodicities were compared to within 1% of precision, yielding no coincidences between the candidates.

3.2. Single-pulse Search

The single-pulse pipeline resulted in a total of 6893 candidate pulses, the majority of which we determined to be erroneous events. Table 3 shows the number of pulses detected per station epoch, $\sigma_{\rm SP}$ thresholds, and representative flux density limits. The large discrepancy in pulse numbers corresponds to a combination of the non-Gaussian noise properties of each data set and the different observing lengths. The ALMA data on April 6 and 11 yield the lowest number of single-pulse candidates; however, on April 7 where there are more instrumental instabilities and residual artifacts in the time series (see Section 2.2 and the Appendix), combined with the longer integration length, a significantly higher number of

Table 4
Parameters from Each Station, Corresponding to the Most Sensitive Data Sets, Used for the Sensitivity Analysis

Station	ν (GHz)	$T^*_{\rm sys}$ (K)	G (K Jy^{-1})	$t_{\rm int}$ (hr)	$\Delta\nu$ (GHz)	ϵ	$S_{\rm min}$ (mJy)	$L^{\rm GC}_{\rm min}$ (mJy kpc^2)	Detected $f_{\rm t}$ (%)	Detected $f_{\rm e}$ (%)
ALMA	228	121	1.054	4.6	3.75	0.05	0.01	0.7	4.1	2.2
LMT	228	490	0.063	3.0	4.0	0.05	1.09	75	0.3	0.1
IRAM 30 m	228	223	0.123	1.1	4.0	0.05	0.42	29	0.4	0.4
ALMA	86	51	1.15	3.0	2.0	0.05	0.01	0.7	n/a	4.0
IRAM 30 m	86–154	125	0.16	3.0	32	0.1	0.06	4.0	1–2	n/a

Notes. Columns indicate the station, observing frequency (ν), average system temperature ($T^*_{\rm sys}$), telescope gain (G), net integration time on-source ($t_{\rm int}$), instantaneous bandwidth ($\Delta\nu$), assumed pulsar duty cycle for the calculations (ϵ), resulting theoretical minimum detectable flux density for $\sigma = 5$ ($S_{\rm min}$), equivalent pseudo-luminosity at the distance of the Galactic center ($L^{\rm GC}_{\rm min}$), and the percentage of the simulated pulsar population in the Galactic center that the observations could detect for the theoretically ($f_{\rm t}$) and empirically derived ($f_{\rm e}$) luminosity limits (see Section 4.2). In all cases, the number of summed polarization $n_p = 2$. The last two rows show the results from similar recent pulsar searches around Sgr A* at wavelengths of 3.5 mm with ALMA (Liu et al. 2021) and 3 to 2 mm with the IRAM 30 m Telescope (Torne et al. 2021), for comparison. The "n/a" abbreviation indicates that a result is not available.

candidates is observed. In general, the LMT and the IRAM 30 m data sets also produced larger numbers of candidates for the same reasons and despite the higher $\sigma_{\rm SP}$ thresholds used.

The analysis of simultaneous events among stations yielded 42 single-pulse candidates coincident within time windows of 86.4 ms or less. Further inspection of the time series around the detected pulses showed that these candidates were produced by baseline level jumps or residual time series artifacts. From the visual inspection of all single-pulse candidates with $\sigma_{\rm SP} > 12$, no convincing real pulses were found.

Using Equation (1) in Karako-Argaman et al. (2015), and the system sensitivity parameters outlined in Table 4, we estimate $\sigma_{\rm SP} = 6$ or $\sigma_{\rm SP} = 10$ on-source sensitivity limits representative of 1, 10, and 50 ms duration single pulses. These limits are outlined in Table 3.

4. Discussion

4.1. Sensitivity of the Periodicity Searches

Several potential factors contribute to the nondetection of pulsars in this search, including the typical steep spectrum of radio pulsars and the far distance to the center of our Galaxy. The sensitivity of a pulsar search is usually quantified by the minimum detectable mean flux density of a pulsar, $S_{\rm min}$, given a certain set of observational and pulsar properties. Based on the radiometer equation, the theoretical sensitivity of a Fourier-domain pulsar search can be expressed following (Cordes & Chernoff 1997):

$$S_{\rm min} = \frac{\beta\,\sigma\,T^*_{\rm sys}}{\eta_{\rm ph} G \sqrt{n_p\,\Delta\nu\,t_{\rm int}}} \left(\frac{1}{\alpha\sqrt{N_h}} \sum_{l=1}^{N_h} R_l \right)^{-1}, \quad (5)$$

where β is a correction factor due to imperfections in digitization ($\beta = 1.136$ in our case for 2-bit sampling; Cooper 1970), $\eta_{\rm ph}$ is the phasing efficiency of a phased array ($\eta_{\rm ph} = 1$ for single-dish telescopes, and $\eta_{\rm ph} \simeq 0.95$ for phased ALMA observations during the EHT 2017 observations; Goddi et al. 2019), σ is the requested detection significance of the pulsar signal, $T^*_{\rm sys}$ stands for the system temperature (including the contribution due to Earth's atmosphere), G is the telescope gain, n_p is the number of summed polarizations, $\Delta\nu$ is the effective observing bandwidth, $t_{\rm int}$ is the integration time, $\alpha \equiv \sqrt{1 - \pi/4}$ is a coefficient related to the rms noise in the Fourier transform of the intensity, N_h is the optimum number of harmonics summed,[172] and R_l is the amplitude ratio of the lth harmonic of the signal to the zero frequency in the Fourier transform. Assuming a Gaussian profile shape of the pulsar signal with a width w (the pulse width at half height of the pulse), R_l can then be written as

$$R_l = e^{-(\pi\epsilon l/2\sqrt{\ln 2})^2}, \quad (6)$$

where $\epsilon \equiv w/P$ is the duty cycle of the pulse. Based on this, the theoretical sensitivities of our searches can be computed using the telescope and data properties summarized in Tables 2, 5, and 5. These results are shown in Figure 2.

In practice, Equation (5) is known to overestimate the realistic sensitivity of a pulsar search. This is particularly true for slow pulsars with large duty cycles, when red noise is prominent in the data (Lazarus et al. 2015; Eatough et al. 2021; Liu et al. 2021). Therefore, a more practical, accurate estimate is obtained empirically by injecting synthetic pulsar signals each time of a different flux density into the real data, conducting the search, and obtaining the minimum detectable flux density. Such a procedure has been carried out using the longest and most sensitive (see Table 5) data set from each of

Table 5
Calibration Information per Station and Epoch

Station	Epoch	G (K Jy^{-1})	$T_{\rm sys}$* (K)	$t_{\rm int}$ (hr)	Γ (μJy)
ALMA	Apr 6	1.054	127	2.1	17
	Apr 7	1.054	121	4.6	11
	Apr 11	1.054	196	1.9	27
LMT	Apr 6	0.033	355	2.4	1294
	Apr 7	0.063	490	3.0	837
	Apr 11	0.067	436	1.7	930
IRAM 30 m	Apr 7	0.123	223	1.1	322

Note. The remaining columns show the telescope gain (G), the average effective system temperature (that includes the contribution due to Earth's atmosphere, $T^*_{\rm sys}$), the net integration time on Sgr A* ($t_{\rm int}$), and a figure-of-merit of the sensitivity of each data set, $\Gamma = 1000 \cdot T^*_{\rm sys}/(\eta_{\rm ph}\,G\,\sqrt{2\,t_{\rm int}\,\Delta\nu})$.

[172] The N_h parameter refers to the number of summed harmonics that minimizes $S_{\rm min}$. It depends on pulse duty cycle and shape (see Appendix A in Cordes & Chernoff 1997, for details). N_h may not coincide with the maximum number of harmonics that the pipeline can sum. The PRESTO pipeline searches for the optimal number of summed harmonics for each detected periodicity up to the limit, which in our case is 32 harmonics.

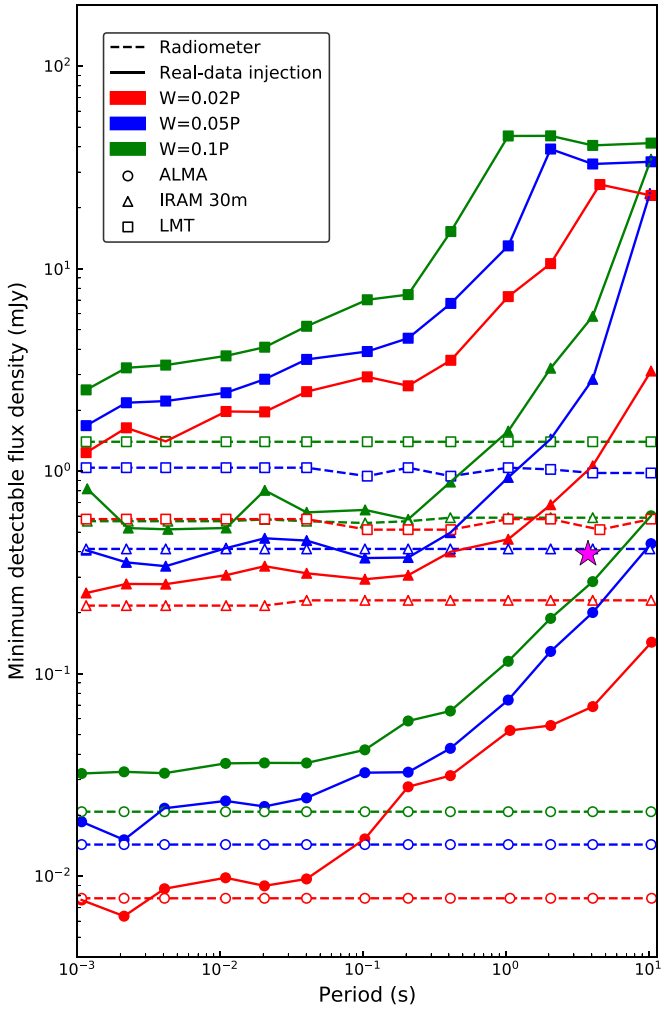

Figure 2. Theoretical (dashed lines) and empirical (solid lines) sensitivity estimates of the search on April 7 (considered the most sensitive in all three epochs) at ALMA, IRAM 30 m, and LMT. The red, blue, and green colors represent injection of signals with 2%, 5%, and 10% duty cycle, respectively. In the empirical estimate, each point represents the median from five injection iterations. The purple star stands for the GC magnetar PSR J1745−2900 using the flux density reported by Liu et al. (2021) and assuming a flat spectrum. Here we used Equation (5) (with $\sigma = 5$) to calculate the theoretical estimate of minimum detectable flux density.

the three telescopes (all on April 7), and the results are presented in Figure 2. It can be seen that for fast-spinning pulsars, the estimate from injection into real data gives a minimum detectable flux density close to the theoretical estimate, compared with those for slow pulsars. As the pulsar period increases, e.g., from 1 ms to 1 s, the empirical sensitivity of the search drops drastically, by up to more than an order of magnitude.

The most sensitive search comes as expected from phased ALMA, where $S_{\rm min} \sim 0.01$ mJy. For the single-dish telescopes, where the field of view is significantly larger, the best sensitivity is yielded by the IRAM 30 m Telescope, where $S_{\rm min} \sim 0.4$ mJy. For the LMT, $S_{\rm min} \sim 1$ mJy. The GC magnetar PSR J1745−2900 had a flux density of 0.39 mJy at 86 GHz on 2017 April 3—the closest published observation, in both epoch and frequency, to those of the EHT (Liu et al. 2021). Under the assumption of a flat spectrum (e.g., Torne et al. 2015, 2017), PSR J1745−2900 would fall below the empirically derived sensitivity limits of both IRAM 30 m and LMT, and would explain our nondetection in the data from these two telescopes (see Figure 2). Although phased ALMA may have had enough sensitivity to detect PSR J1745−2900 during the EHT 2017 observations, its field of view of 1″–2″ was not wide enough to cover this source.

The sensitivity estimates given above are primarily for the Fourier-domain search methods. The sensitivity of the FFA is in theory on a similar level. In Morello et al. (2020), the theoretical sensitivity difference between these two methods is characterized by the search efficiency factor ($\mathcal{E}$), a function of the number of harmonics summed and duty cycle of the pulsar. With a summation of up to 32 harmonics, this factor is approximately 0.65, 0.76, and 0.83 for signals with duty cycles of 2%, 5%, and 10% (used in our estimates above), respectively. Assuming $\mathcal{E}_{\rm FFA} = 0.93$ as in Morello et al. (2020), the theoretical sensitivity of the FFA search is better than the FFT search by factors of 1.4, 1.2, and 1.1, respectively.

Finally, to illustrate the advantage of our search at very high frequency to overcome the scattering effect, we consider a pessimistic (but still possible) scenario of temporal scattering toward the GC as predicted by the NE2001 model, i.e., $\tau_{\rm s} = 2000\,\nu^{-4}$ s (ν in units of gigahertz), where $\tau_{\rm s}$ is the exponential characteristic time on the pulses due to the scattering, and ν is the observing frequency. Even in this case, at 228 GHz the scattering time would be $\tau_{\rm s} \approx 740$ ns, roughly 40 times smaller than our smallest sampling interval, 3 orders of magnitude less than the spin period of any pulsar known, and ∼50 times less than the narrowest pulse width known to date (Manchester et al. 2005). We note that the scattering measured for the currently known closest pulsar to Sgr A*, PSR J1745−2900 ($\tau_{\rm s} \simeq 1.3\nu^{-3.8}$; Spitler et al. 2014), is much smaller than the predicted value from the NE2001 model. However, we cannot fully discard a patchy environment in the innermost region of the Milky Way, with different scattering for different lines of sight due to multiple screens (e.g., Schnitzeler et al. 2016; Dexter et al. 2017). In any case, due to the very-high observing frequency of the EHT, our search sensitivity is unaffected by interstellar scattering.

4.2. Potential of the Search to Detect a Galactic Center Pulsar Population

Once the flux density limits of the observations are known, we can estimate the potential to detect pulsars around Sgr A* with this search. We do this by calculating how many pulsars, from a simulated population in the GC, would be detectable with our actual sensitivity. In the following analysis, we focus on the most sensitive observation from each station as representative of the best limit for GC pulsar detectability, i.e., the data from April 7 (see Table 5).

The flux density limit from Equation (5) or through the injection of signals (Section 4.1) can be converted to a pseudo-luminosity limit at the GC by multiplying $S_{\rm min}$ by the square of the distance to the GC (see, e.g., Lorimer & Kramer 2004), $d_{\rm GC} = 8.28$ kpc (Gravity Collaboration et al. 2021):

$$L_{\rm min}^{\rm GC} = S_{\rm min}\, d_{\rm GC}^2 = S_{\rm min}\, 8.28^2\ [\text{mJy kpc}^2]. \quad (7)$$

The simulated population in the GC is created from the known pulsar population in the Milky Way, i.e., we assume that the putative pulsars at the center of the Galaxy resemble in properties those of the Milky Way. Although the properties of the pulsars that may populate the innermost region of the

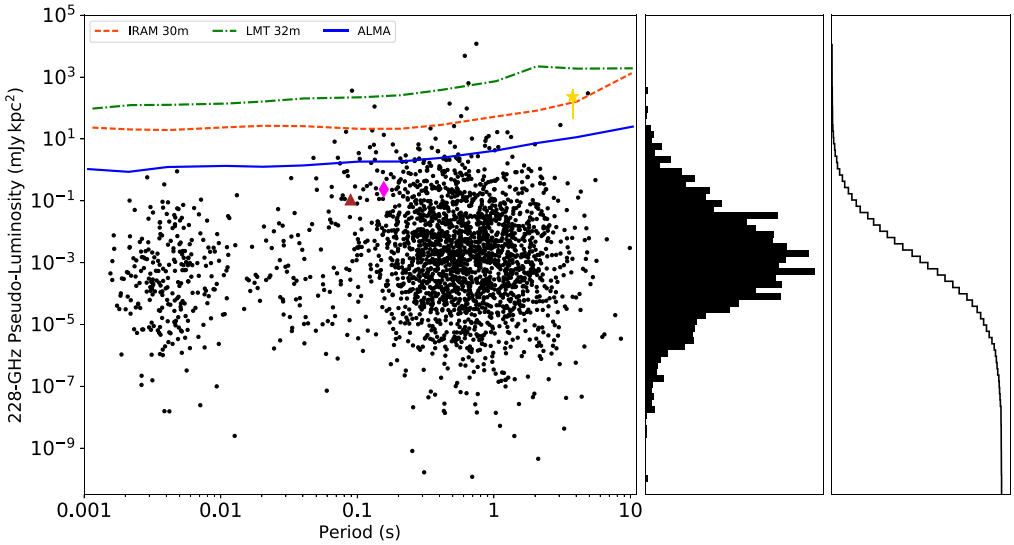

Figure 3. Left panel: luminosity of the simulated pulsar population at 228 GHz (black dots) with the empirically derived minimum detectable luminosity for each telescope at the distance to the GC ($d = 8.28$ kpc) overplotted as lines. The minimum detectable luminosity corresponds to the empirical limits on flux density as seen in Figure 2 for a pulse duty cycle of 5%. The blue line, dashed–dotted green line, and dashed orange line represent the limits for ALMA, LMT, and the IRAM 30 m Telescope, respectively. Each black dot represents a simulated pulsar, and the dots above each line would in theory be detectable for that telescope. For reference, PSR J1745−2900's average luminosity at 228 GHz (Torne et al. 2015, 2017), the Vela pulsar (PSR B0833−45), and PSR B0355 + 54 are marked with a yellow star, brown triangle, and pink diamond, respectively. The vertical line over the yellow star marks the range of known variability of PSR J1745−2900. Middle: histogram of the luminosity distribution. Right: histogram of the luminosity distribution in a cumulative layout.

Galaxy are unknown, we consider this is a valid assumption given that both old and new populations of stars exist in the GC (Pfuhl et al. 2011; Nogueras-Lara et al. 2022). We use the pulsar catalog PSRCAT[173] (Manchester et al. 2005) version 1.67, extracting the pseudo-luminosity of those pulsars for which this value is available (in this catalog version, from 3320 pulsars, 2457, i.e., 74%, have a pseudo-luminosity entry). These pseudo-luminosity values are, in most cases, provided for frequencies of 400 and 1400 MHz. We therefore extrapolate to 228 GHz by using the spectral index of each pulsar that is available in the catalog. When the spectral index is not available, we draw a sample from a normal distribution with mean value $\langle \alpha_1 \rangle = -1.60 \pm 0.54$ (Jankowski et al. 2018). Both when the spectral index is known and when we draw from the distribution, a single power law for the extrapolation is used. Finally, we compute the percentage of pulsars with an extrapolated pseudo-luminosity at 228 GHz above the pseudo-luminosity limit obtained with Equation (7), both with the theoretically and empirically derived $S_{\rm min}$. Those percentages of the simulated pulsars would be in theory detectable in this search.

Because the exact number of pulsars above the limit will depend on the samples drawn from the normal distribution of spectral indices, we run a Monte Carlo simulation with 10,000 executions to obtain the average percentage of detectable population for each station. A summary of the utilized parameters and the results are presented in Table 4. Figure 3 shows a snapshot of the Monte Carlo simulation (representative of the results), together with the empirical luminosity limits for each station.

In addition, to investigate how the spectral index distribution could affect the results, we repeated the analysis in other scenarios for the simulated pulsar population: one with $\langle \alpha_2 \rangle = -1.4 \pm 1.0$ (Bates et al. 2013), and with $\langle \alpha_3 \rangle = -1.8 \pm 0.2$ (Maron et al. 2000). Similarly, the impact of the duty cycle parameter was evaluated by repeating the simulation, only for the spectral index distribution $\langle \alpha_1 \rangle$, for $\epsilon = 0.01$, and 0.2.

Focusing on the results from the empirical sensitivity, the spectral index distribution $\langle \alpha_2 \rangle$ results in a detectable percentage of the simulated population of 8.8%, 1.3%, and 3.4% for ALMA, LMT, and the IRAM 30 m Telescope, respectively. In the case of using $\langle \alpha_3 \rangle$, the percentage decreases to 1.4%, 0.1%, and 0.3%, respectively. These results show that the percentage of detectable population can vary by a factor ∼2–10 depending on the spectral index distribution utilized—mainly a result of the required extrapolation to 228 GHz and the difference in the standard deviation of the assumed distribution. The simulations show that the mean value itself has a smaller impact on the result than the standard deviation. Even with a steeper mean value, if the standard deviation is sufficiently large, pulsars with flat spectral indices and thus more likely emitting above our sensitivity threshold at 228 GHz, will be drawn from the distribution. In the future, better understanding the distribution of pulsar spectral indices at high radio frequencies ($\nu \gtrsim 20$–30 GHz) would help to obtain more accurate estimations for the potentially detectable fraction from pulsar searches at very high radio frequencies (see Löhmer et al. 2008). In contrast, the simulations with additional values of the duty cycle $\epsilon = 0.01$ and 0.2 in the $\langle \alpha_1 \rangle$ scenario shows negligible variations on the detectable population.

The first conclusion from the results summarized in Table 4 is that our potential to detect pulsars in the GC with this search is in general low. This was somewhat expected, primarily due to the effect of the average steep spectral index of pulsars. However, with the observations at 228 GHz, we were mainly targeting flat-spectrum pulsars, like radio magnetars, and probing a frequency space where certain emission models include possible emission boosts, making certain pulsars

[173] https://www.atnf.csiro.au/research/pulsar/psrcat/

potentially visible. Furthermore, the single-pulse analysis may detect pulsars through bright single pulses.

A second finding shows that the percentage of detected pulsars can decrease by up to ∼50%–60% when using the empirically derived sensitivity limits versus the theoretical ones. This sensitivity loss is substantial, and is caused by the noise characteristics, which are far from showing the Gaussian statistics that the radiometer equation assumes. From the three stations, the data from the IRAM 30 m seems to be less affected by this loss of sensitivity. This is apparent in Figure 2, where the empirical limit for this station is flatter, and starts rising at longer spin periods as compared to the ALMA and LMT cases.

The highest fraction of detectable population in the EHT 2017 data comes from ALMA, which, despite its superb sensitivity, could detect only around 2.2% of the brightest pulsars in the simulated population with $\langle\alpha_1\rangle$—that we consider as the most accurate. This fraction is lower by a factor ∼2 compared to the one yielded by ALMA in 2017 Global Millimeter very long baseline interferometry (VLBI) observations, of about 4%, despite the use of only 2 GHz of bandwidth (Liu et al. 2021). In the case of the IRAM 30 m Telescope and the LMT, less than 0.4% and 0.1% of the simulated pulsars, respectively, would be detectable with the EHT 2017 data. For the IRAM 30 m, previous searches at 3 and 2 mm yielded theoretical population coverage fractions of 1%–2% (Torne et al. 2021). The differences arise from a combination of different search parameters (e.g., $T_{\rm sys}{}^{*}$, G, $t_{\rm int}$, or $\Delta\nu$), together with the higher average luminosity of pulsars at the longer wavelengths.

Focusing on the EHT 2017 data, the simulations show therefore that only a very small number of very bright pulsars at 228 GHz (1.3 mm), i.e., those that not only are bright but also show a flat (or inverted) spectrum, had chances to be detected in this search. In fact, even bright pulsars at centimeter wavelengths like Vela, and bright, relatively flat-spectrum pulsars like PSR B0355+54, would not be detected in our survey if located at the GC. Consequently, it is not surprising that no detections of new pulsars were achieved by our search. Related to our low sensitivity, it is therefore plausible that pulsars emitting below our current luminosity limits exist in the region. This is particularly relevant for MSPs, which may be less luminous than normal pulsars (e.g., Bailes et al. 1997; Kramer et al. 1998). From our simulations, our sensitivity to MSPs in this search is close to zero (see Figure 3). Given that the GC may be dominated by an MSP population (Gordon & Macias 2013; Macquart & Kanekar 2015; Schödel et al. 2020), this could also explain the lack of discoveries.

We remark that even pulsars emitting above our detection limits and with orbital parameters within the searching pipelines capabilities (see Section 4.3) may be missed by other factors. For example, a pulsar could be highly variable in flux density (as occurs with radio-emitting magnetars; see, e.g., Torne et al. 2017), or eclipses due to surrounding gas could hide a pulsar emission for some periods of time in binary systems (e.g., Freire 2005). Relativistic precession can move the beam of emission of a pulsar orbiting a companion in and out our line of sight (e.g., Kramer 1998; Perera et al. 2010). These reasons alone justify repeated surveys for pulsars around Sgr A* at different epochs separated in time to overcome these time-dependent effects.

Lastly, another case potentially affecting our sensitivity is when a pulsar's spin and orbital parameters are beyond the capabilities of our pipelines to recover the accelerated signals. This mostly affects fast MSPs ($P \lesssim 5$ ms) in tight orbits around massive companions. Nevertheless, the possibility that the center of the Galaxy is populated to a large extent by MSPs cannot be ruled out (e.g., Rajwade et al. 2017). Since the main signals aimed for here are pulsars orbiting the SMBH Sgr A*, we should consider our sensitivity to such MSP-(SM)BH systems potentially lower than the limits shown in Table 4 and Figures 2 and 3. In the next section, we discuss this relationship between sensitivity and binary systems in more detail.

4.3. Search Capability for Pulsars in Various Orbits around Sgr A*

The phased ALMA field of view is significantly smaller than LMT and IRAM 30 m, sampling a smaller volume and range of potential orbits near Sgr A*. Using the distance and mass of Sgr A* derived from Gravity Collaboration et al. (2021) and assuming a circular orbit, the phased ALMA field of view is able to cover an orbital period of approximately up to $P_{\rm b} \approx 300$ yr. This is already enough to cover a large fraction of the stars known to date in the S-star cluster (Sabha et al. 2012; Gillessen et al. 2017), and certainly also the orbits that would enable Sgr A* measurements and gravity tests with pulsars (Liu et al. 2012). Meanwhile, the field of view of LMT and IRAM 30 m can cover orbital periods of up to $P_{\rm b} \approx 4000$ yr. So, even though their observations are less sensitive, the LMT and IRAM 30 m Telescope are able to cover a significantly larger volume of any putative pulsar population in the GC.

In practice, as already mentioned in Section 2.3, the range of acceleration and its derivative explored in the search would also place a constraint on the types of orbits around Sgr A* that the search is able to detect. For a given time span of the observation, the constraint can be estimated by calculating the maximum absolute z- and w-values in a range of orbits and comparing with those used in the search, as demonstrated in Liu et al. (2021; see also Eatough et al. 2021). Here, as case studies, we carried out the same practice for two time spans of the observation, $T_{\rm obs} = 10.2$ and 3.2 hr, which correspond to the April 7 observation of ALMA and IRAM 30 m, respectively, being the longest and shortest time spans in our data set. We focus on a full sensitivity signal recovery based on 32 summed harmonics (see Section 2.3.1). The results are summarized in Figure 4, with a selection of two typical spin periods for ordinary pulsars ($P \simeq 500$ ms) and MSPs ($P \simeq 5$ ms), respectively.

With the settings detailed in Section 2.3.1, our search using 10.2 hr long data is capable of detecting ordinary pulsars well within 1 yr orbits around Sgr A*, likely down to $P_{\rm b} \gtrsim 0.5$ yr. For MSPs, we are able to detect those with an orbital period longer than 10 yr. Meanwhile, the search using 3.2 hr long data can detect ordinary pulsars in much closer orbits, i.e., down to 0.2 yr (≈2.4 months). For MSPs, it can detect orbits with as short as approximately 2 yr periods. These are also inferred by Equations (3) and (4), where the parameter space in acceleration and jerk to be explored scales down for short observations and slow pulsars. Note that as shown in Table 1, the ALMA observations from April 6 and 11 have a similar time span and thus coverage of pulsar orbits as the IRAM 30 m observation.

As discussed in Liu et al. (2021), the above limit estimate on the orbits corresponds to the boundary where the optimal

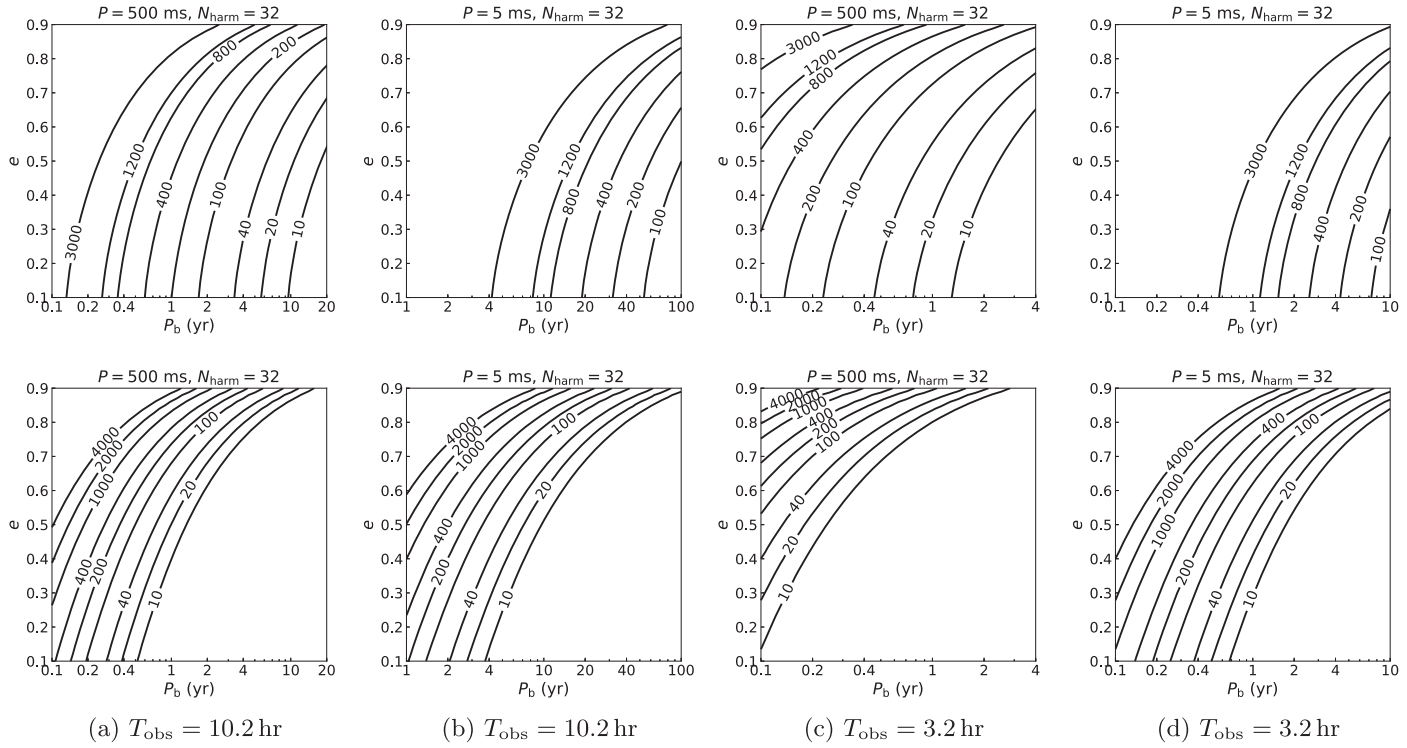

(a) $T_{\rm obs} = 10.2\,{\rm hr}$ (b) $T_{\rm obs} = 10.2\,{\rm hr}$ (c) $T_{\rm obs} = 3.2\,{\rm hr}$ (d) $T_{\rm obs} = 3.2\,{\rm hr}$

Figure 4. Values of `zmax` (upper row) and `wmax` (lower row) required for the Fourier-domain search to be conducted with optimal sensitivity in orbits around Sgr A* with different periods and eccentricity (e). Here we use two pulsar spin periods, which are typical values for ordinary pulsars and MSPs, respectively. The time spans of the observations are assumed to be 10.2 and 3.2 hr, which are in turn the longest and shortest in our analyzed data sets.

sensitivity can always be retained throughout the entire orbit. If, in practice, the search conducted does not cover the recorded $\max(|z|)$ and $\max(|w|)$, it would start to lose sensitivity in the worse scenario but could still detect the pulsar. For instance, for highly eccentric orbits, the pulsar spends most of the time near apoastron, where the acceleration and its derivative are considerably lower than those near periastron. In this case, searches that do not cover $\max(|z|)$ and $\max(|w|)$ of the entire orbit could still be capable of finding the pulsar at a large fraction of the orbital phase.

4.4. Constraints on a Putative Galactic Center Pulsar Population

Theoretical estimations on the number of pulsars that may exist in the inner part of our Galaxy differ considerably, with typical assumed values from around ∼200 (Chennamangalam & Lorimer 2014) to thousands (Wharton et al. 2012). The wide range relates mainly to the complexity and peculiarity of the star-forming history and evolution in the GC, and the dynamics that the high-density environment and the SMBH introduce (see, e.g., Figer 2009; Morris 2023). Using our survey results, we can try to constrain the number of pulsars that may exist in the GC.

We will assume a population of pulsars located at the distance of Sgr A*. For simplicity in the calculations, the population will have a Gaussian radial distribution, with two parameters: n_0 as the number density of pulsars, and $\sigma_{\rm R}$ the rms radial scale, for a 3D Gaussian distribution. Following a similar approach as in Cordes & Chernoff (1997), integrating over the angles sampled by each telescope, we calculate the mean expected number of pulsar detections from this assumed population ($N_{\rm d}$), for a given telescope, as

$$N_{\rm d}(n_0,\,\sigma_{\rm R}) = (2\pi)^{3/2}\, n_0 \left[\frac{f_{\rm s}\;{\sigma_{\rm R}}^3}{1 + {\sigma_{\rm R}}^2/(d_{\rm gc}\sigma_\theta)^2}\right], \qquad (8)$$

where $f_{\rm s}$ is the fraction of detectable pulsars with a given telescope (we use the empirical detection fraction $f_{\rm e}$ for our calculations; see Table 4), $d_{\rm gc}$ is the distance to the GC, and σ_θ is the rms angular scale of a Gaussian beam pattern for the telescope.

To constrain the parameters of the population, we assume that our probability for detections follows a Poisson distribution. Given our nondetections, we build our survey likelihood function as $\mathcal{L}_0 = P_0 = e^{-N_{\rm d}}$. We note that the two parameters for the assumed GC pulsar population are not statistically independent, so the upper limits for n_0 will depend on $\sigma_{\rm R}$. We calculate an upper limit for $N_{\rm d}$ (and so, also for n_0) at a given confidence level, that we choose here as 99.7%. In order to obtain the most stringent constraint on the expected number of pulsars, we select the lowest n_0 for each $\sigma_{\rm R}$ from the values obtained from the three used telescopes. Finally, we compute an upper limit for the expected mean number of total pulsars in the assumed population as $N_{\rm psr}^{\rm GC} = n_0\, V_{\rm pop}$, where $V_{\rm pop} = (2\pi)^{3/2}\,\sigma_{\rm R}^3$ is the volume enclosing the assumed population. The results are plotted in Figure 5.

Although we have not detected any pulsar in the EHT 2017 observations, we know that at least one pulsar exists near Sgr A*: the magnetar PSR J1745−2900, just 3″ away (i.e., a projected distance of ≈0.1 pc; Rea et al. 2013). This pulsar was not detected because it is highly variable and was likely on a weak-emission state during the EHT 2017 campaign. PSR J1745−2900 would have been detected by the IRAM 30 m Telescope, and even phased ALMA (even offset from the

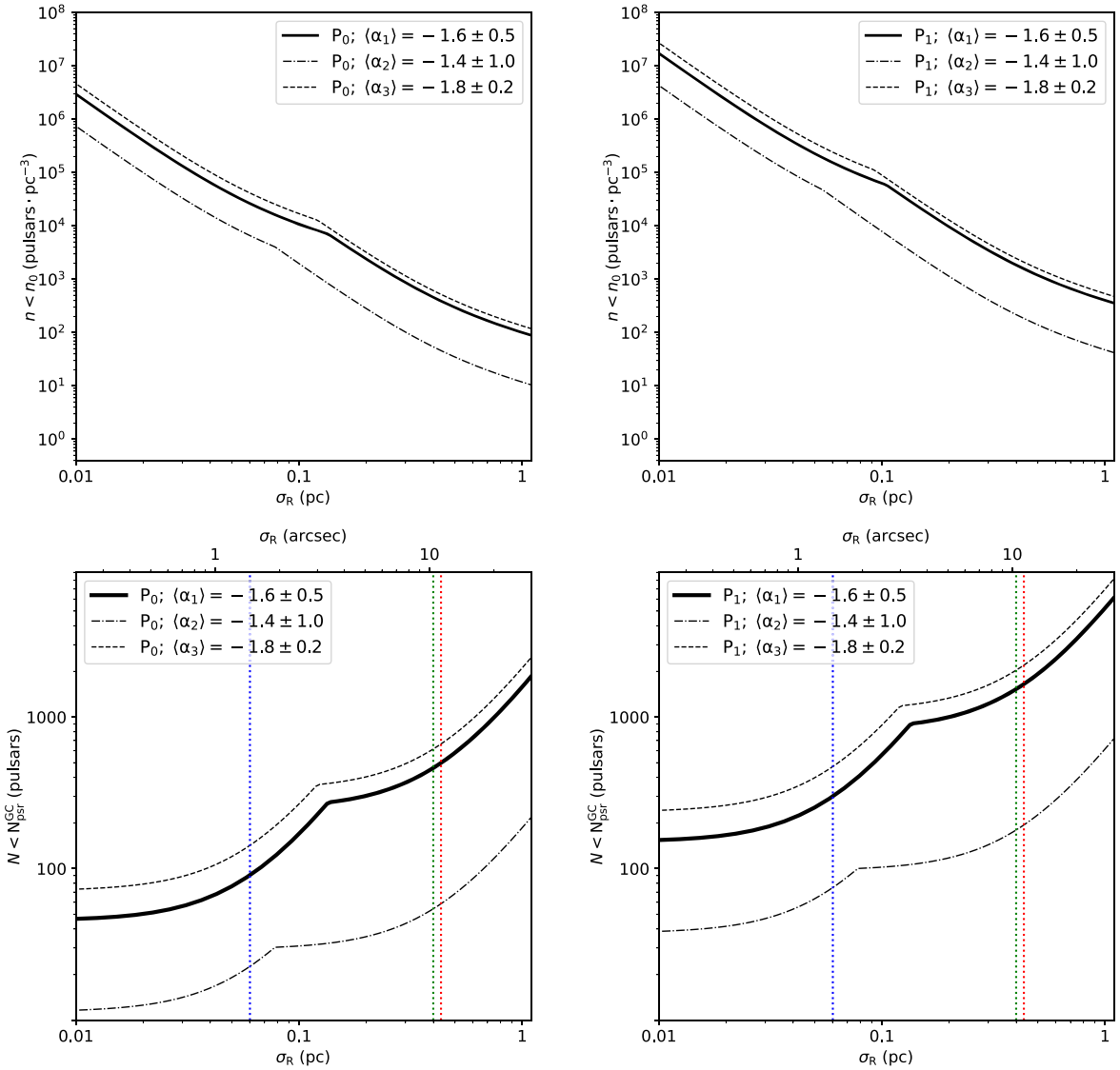

Figure 5. Top panels: upper limits on pulsar number density (n_0) vs. Gaussian radial width (σ_R) constrained by the EHT 2017 observations for a survey likelihood $\mathcal{L}_0 = P_0$ (left) and $\mathcal{L}_1 = P_1$ (right). Bottom panels: upper limit on the number of expected pulsars around Sgr A* within a spherical Gaussian volume with radial width σ_R. The top axis indicates the Gaussian radial width in arcsecond scale, for easier comparison with the telescope beam sizes, represented by the vertical dotted lines in blue, green, and red, at ≈0.06, ≈0.4, and ≈0.43 pc for phased ALMA, LMT, and the IRAM 30 m, respectively. The survey likelihood function is $\mathcal{L}_0$ (left) and $\mathcal{L}_1$ (right). In all of the panels, the continuous thick, dotted–dashed, and dashed lines marks the upper limits for a pulsar population with a mean spectral index $\langle\alpha_1\rangle$, $\langle\alpha_2\rangle$, and $\langle\alpha_3\rangle$, respectively.

center of its synthetic beam), if it were in a bright-emission episode (PSR J1745−2900 can reach $S \sim 6$ mJy at 1.3 mm; Torne et al. 2017). Taking into account an alternative scenario with a detection of PSR J1745−2900, we also present the upper limits considering our survey likelihood function $\mathcal{L}_1 = P_1 = N_d\, e^{-N_d}$ in Figure 5.

The derived upper limits show that, given the assumptions made on GC pulsar population properties (i.e., similar in properties to the known pulsar population, and with the chosen spectral index distribution $\langle\alpha_1\rangle = -1.60 \pm 0.54$), and the characteristics of the telescopes used, of the order of thousands of pulsars can populate the GC if distributed in a region of width ∼1 pc or more around Sgr A*. For instance, if the pulsars are assumed to exist within the inner central pc ($\sigma_R = 1$ pc), $N_{psr}^{GC} \lesssim 1600$ ($N_{psr}^{GC} \lesssim 5300$ in the case of using $\mathcal{L}_1$). A scenario of particular interest is when the assumed pulsar population in the GC is very compact around Sgr A*, within a volume containing (circular) pulsar orbital periods $P_b \lesssim 100$ yr around Sgr A*. This smaller volume encloses the most promising pulsars for gravity tests with Sgr A* (Wex & Kopeikin 1999; Pfahl & Loeb 2004; Liu 2012), and is given by a $\sigma_R \approx 0.02$ pc, yielding $N_{psr}^{GC} \lesssim 50$ ($N_{psr}^{GC} \lesssim 160$ in the case of using $\mathcal{L}_1$). Our results therefore cannot set stringent constraints on the number of pulsars in the inner parsec of the galaxy, mainly due to our low sensitivity at large radial scales (constrained by the wider beams of IRAM 30 m and LMT). However, on smaller radial scales ($\sigma_R \lesssim 0.1$ pc), phased ALMA offers better sensitivity. In these smaller scales, we are still compatible with a population of tens to hundreds of pulsars close to the central SMBH and beamed toward us.

We note however that N_{psr}^{GC} is subject to big uncertainties. One of the largest ones arises from the assumption made on the properties of the pulsars that may exist in the GC, from which the detection fraction, f_s, is derived. To illustrate the impact of just a

different mean spectral index taken for the GC pulsar population, the upper limit for $N_{\rm psr}^{\rm GC}$ for a population within 1 pc around Sgr A* varies between $N_{\rm psr}^{\rm GC} \lesssim 190$ and $N_{\rm psr}^{\rm GC} \lesssim 2100$ ($N_{\rm psr}^{\rm GC} \lesssim 620$ and $N_{\rm psr}^{\rm GC} \lesssim 7100$ if $\mathcal{L}_1$) for the spectral index distributions $\langle\alpha_2\rangle = -1.4 \pm 1.0$ and $\langle\alpha_3\rangle = -1.8 \pm 0.2$, respectively. In the case of a compact population enclosed within 0.02 pc around Sgr A*, $N_{\rm psr}^{\rm GC}$ varies between $N_{\rm psr}^{\rm GC} \lesssim 10$ and $N_{\rm psr}^{\rm GC} \lesssim 75$ ($N_{\rm psr}^{\rm GC} \lesssim 40$ and $N_{\rm psr}^{\rm GC} \lesssim 250$ if $\mathcal{L}_1$), again for $\langle\alpha_2\rangle$ and $\langle\alpha_3\rangle$, respectively. The upper limits on $N_{\rm psr}^{\rm GC}$ for the scenarios with mean spectral indices $\langle\alpha_2\rangle$ and $\langle\alpha_3\rangle$, for comparison, are also shown in Figure 5.

Finally, we remark that the upper limit $N_{\rm psr}^{\rm GC}$ refers to pulsars active in radio and beamed toward us. The limits for total number of neutron stars in the assumed regions would be considerably greater depending on the assumed beaming fraction and ratio of radio-active neutron stars over all of the existing ones. For instance, for a mean beaming fraction of 0.1 (Faucher-Giguère & Kaspi 2006) and a ratio of radio-active over all neutrons stars of 10^{-2}–10^{-3} (Faucher-Giguère & Kaspi 2006; Keane & Kramer 2008; Sartore et al. 2010), the upper limits for neutron stars would scale up by a factor $\mathcal{O}(10^3$–$10^4)$. Therefore, despite our nondetections, our results are consistent with a large population of neutron stars in the GC, and are compatible with results from theoretical simulations and population synthesis (Alexander 2017; Baumgardt et al. 2018; Gravity Collaboration et al. 2020; Chen et al. 2023).

5. Future Improvements

5.1. Flux Density Sensitivity

The pulsar search in this paper used EHT 2017 campaign data with a total bandwidth of $\Delta\nu \approx 4$ GHz. Later EHT observations, starting from 2018, began to record an instantaneous bandwidth of $\Delta\nu = 8$GHz, offering a factor of $\sqrt{2}$ improvement in system sensitivity. Additionally, for single-dish telescopes, observing in the VLBI mode requires a notably larger overhead compared to those in stand-alone mode, as a result of the time spent on phase calibrators and the associated slewing time (see Table 1). For the same observing length, dedicated pulsar surveys would largely increase the fraction of time spent on Sgr A*, by possibly more than a factor of 2; this would improve the system sensitivity by roughly another factor of 1.5.

Furthermore, in this work we searched the data sets individually, which were in fact collected from simultaneous observations at different telescopes. In principle, it is possible to increase the search sensitivity by coherently summing the data collected with the entire EHT array, forming tied array beams toward areas in the vicinity of Sgr A* (see, e.g., Bassa et al. 2016). This may also effectively mitigate some of the systematics present in individual telescope data because they should not correlate between stations. A downside is that a large number of beams needs to be formed, which requires substantial computing power. For instance, given the longest baseline of the EHT 2017 observation, of the order of 20 million beams would be needed to cover an area of 0.″1 around Sgr A*. These beams will also have to be contained by the smallest beam in the array, which is the synthetic beam of ALMA for the EHT 2017 campaign. This could be improved if multibeaming capability of ALMA becomes available.

Table 6
Equivalent Diameter Delivered by a Variety of Summation Forms of the EHT Array

Telescope Combination	Diameter (m)
ALMA	74
LMT	50
Coherent, ALMA+LMT+NOEMA+PV	107
Coherent, all single dishes	64
Coherent, all	111
Incoherent, ALMA+LMT+NOEMA	80
Incoherent, all single dishes	52
Incoherent, all	81

Note. The equivalent diameters of each individual telescope are obtained from Event Horizon Telescope Collaboration et al. (2019d).

To improve the feasibility of coherent beam forming of the EHT array, the beams can be directed toward compact objects that may be identified by imaging observations. Alternatively, incoherently adding the data and/or coherently summing only a subset of the array may also be considered as an option to increase the system sensitivity. Table 6 summarizes the delivered equivalent diameters of the array under different ways of summing the telescope signals. For coherent addition, the summation of the entire array will deliver a sensitivity equivalent to a 111 m dish, while summing only the most sensitive four telescopes in the array will still yield an equivalent diameter of 107 m, only 7% less in sensitivity.

The sky area where a coherent beam may be formed is restricted by the smallest beam size of the array, which is from one of the interferometers. If summing only the single-dish telescopes, the sky coverage can then be enlarged to the smallest beam size of the single dishes. This will give an equivalent diameter of 64 m, approximately 60% more sensitive than LMT, the largest single dish in the array. For incoherent summation, adding the data from the entire array will give an equivalent diameter of 81 m. However, only a few percent difference is expected from summing only the top three sensitive telescopes, i.e., ALMA, LMT, and the NOrthern Extended Millimeter Array (NOEMA).[174] Similarly, incoherent summation of all single-dish telescopes in the array will deliver an equivalent diameter of 52 m—only 8% improvement in sensitivity from the LMT. This is largely due to the significant difference in gain among the telescopes.

Finally, the sensitivity of the LMT during the EHT 2017 campaign is far from its full capacity, mainly due to the under-illumination of its surface. It is expected that the LMT data from later EHT observations will deliver much higher sensitivity.

5.2. Orbital Parameters and Searching Algorithms

As discussed in Section 4.3, the acceleration search performed in this work has optimal sensitivity for pulsars in a certain range of orbits. To cover more compact orbits with Sgr A* optimally, or where a fast MSP is involved, it is possible to simply increase the range of acceleration and jerk used in the search (at the expense of higher computational costs).

[174] NOEMA, a twelve 15 m antennas interferometer located in the French Alps, with phasing capabilities offering an equivalent single-dish diameter $D_s \approx 52$ m, joined the EHT array in 2018.

Alternatively, new searching schemes could also be introduced to directly explore the space of Keplerian parameters (e.g., Balakrishnan et al. 2022), delivering optimal sensitivity to more types of orbits. Nonetheless, the challenge for these search strategies is the computing power required, considering that pulsar orbits in the high stellar density region of the GC are expected to be significantly eccentric. As such, the full set of five parameters is required to describe the orbit rather than only three for circular orbits.

Another possible approach to enable optimal sensitivity for more compact orbits is to divide up the entire length of data into segments and to search each segment individually (Ng et al. 2015; Eatough et al. 2021; Liu et al. 2021). Admittedly, this approach suffers from a loss in sensitivity due to shorter integration times in each segment, but it is more computationally feasible.

5.3. Data Cleaning and Quality

The impact of red noise is a major source of sensitivity loss in pulsar searches, particularly detrimental in high radio frequencies, where the instrumentation and opacity variations produce an excess of power in the low-frequency end of the Fourier spectrum. This effect combines with the fact that radio magnetars, usually found slowly spinning, are one of the main targets of pulsar surveys in the short millimeter range, due to their typically flat spectrum. An optimal red noise reduction scheme can improve the sensitivity of our surveys, although the exact filtering and parameters required are nontrivial and depend on the data properties and the specific properties of the pulsars to be detected (Singh et al. 2022). Future surveys may need different passes with a suite of red noise filtering techniques to optimize the results.

Extra improvements in sensitivity to pulsars could potentially come from the reduction of the locally generated signals that exist in the data. The SIS receivers themselves and the downconversion systems in the (sub)millimeter telescopes are complex, with many oscillators and mixers, and therefore can introduce external signals into the final data recorded to disk. These local signals are often highly periodic. This is generally not an issue for spectroscopic or continuum observations, where the scans are shorter in integration length, and the data are averaged over a comparatively longer time as compared to the data analyzed here for the pulsar search.[175] Nonetheless, in the case of using the data for a search for pulsars, such local periodic signals can have a substantial impact on the sensitivity.

The detrimental effect comes mainly from large excesses of power in many Fourier bins, which then interfere with the searching algorithms by the extra candidates found. Although local interfering signals (both internal and external to the telescope system) are common in radio observations, they can be particularly harmful at very high radio frequencies, where the dispersion effect is very small or negligible.[176]

5.4. Other Wavelengths

In addition to the presented search at $\lambda = 1.3$ mm ($\nu = 228$ GHz), efforts to survey the GC pulsars using modern receivers were done at both centimeter ($\nu \simeq 4$ to 20 GHz; Macquart et al. 2010; Eatough et al. 2021; Suresh et al. 2022) and short millimeter wavelengths ($3 \gtrsim \lambda \gtrsim 2$ mm, $\nu \simeq 80$ to 160 GHz; Liu et al. 2021; Torne et al. 2021), with no discoveries of pulsars.

With risk of still having a strong scattering affecting the centimeter-wavelength observations, and with the large impact on sensitivity by the steep spectrum of pulsars at the short millimeter wavelengths, attempting new surveys with high sensitivity in the short-centimeter- and long-millimeter-wavelength regime is compelling. Such a frequency range (around ~10–50 GHz) would still diminish the scattering and dispersive effects of the interstellar medium, while observing in a spectral window with stronger emission from the steep-spectrum pulsars. This range may contain the frequency "sweet spot" between scattering mitigation and sensitivity to pulsars near Sgr A* (Macquart et al. 2010; Macquart & Kanekar 2015; Bower et al. 2018).

6. Summary and Conclusions

We carried out a search for pulsars and fast transients in the GC with the 2017 Event Horizon Telescope observations, the first search at an observing wavelength of $\lambda = 1.3$ mm ($\nu = 228$ GHz). The search used data from phased ALMA, LMT, and the IRAM 30 m Telescope, the most sensitive telescopes in the EHT array of 2017. Periodicity searches both in the Fourier domain and with an FFA were conducted to each individual data set collected on three different nights, with acceleration and jerk search incorporated to cope with the potential orbital motion of pulsars around Sgr A* or a binary companion. Single-pulse searches were also performed to the whole data set.

These searches did not detect any pulsars or transients. We estimated the search sensitivity both theoretically and in practice by injecting artificial signals into the real data. The practical sensitivities for fast-spinning pulsars ($P = 1$–10 ms) are approximately 0.02, 0.4, and 1 mJy for ALMA, the IRAM 30 m Telescope, and LMT, respectively, but are roughly an order of magnitude worse for slow pulsars ($P = 1$–10 s). In addition, we showed the possible pulsar orbits that can be detected with our searching scheme. We explored the detectability of the search toward a simulated pulsar population in the GC and around Sgr A*, concluding that the sensitivity of the observations is still low. For MSPs in particular, which may be a dominant population in the region, the search sensitivity is close to zero. The lack of discoveries is therefore not indicative that pulsars do not exist in the region; there could still be pulsars in the covered areas that simply emit below our detection thresholds. Finally, we discussed future improvements that can be introduced to optimize the usage of these and similar data, to improve the system sensitivity, and, overall, the chances for the detection of pulsars that likely still hide in the vicinity of the SMBH Sgr A*.

Acknowledgments

We are grateful to the anonymous referee for the review and providing suggestions that improved the manuscript. We thank the staff at the participating observatories and correlator centers that made possible the EHT 2017 observations. P.T. thanks Pablo Mellado and William Robertson for their support through several stages of the data reduction in the IRAM servers. R.P.E. is funded

[175] As an example, typical spectroscopic observations use a sampling time longer than ~100 ms, which "dilutes" many of the fast periodic signals detected in a microsecond-order sampled data.

[176] At low radio frequencies, the de-dispersion step in a pulsar searching algorithm smears the power of broadband local signals, decreasing their impact in the detection of celestial signals by allowing us to discern which broadband signals have traveled though the interstellar medium.

by the Chinese Academy of Sciences President's International Fellowship Initiative, grant No. 2021FSM0004. S.M.R. is a CIFAR Fellow and is supported by the NSF Physics Frontiers Center awards 1430284 and 2020265. This work was supported by the European Research Council Synergy Grant "Black-HoleCam: Imaging the Event Horizon of Black Holes" (grant 610058). This paper makes use of the following ALMA data: ADS/JAO.ALMA#2016.1.01404.V. ALMA is a partnership of the European Southern Observatory (ESO; Europe, representing its member states), NSF, and National Institutes of Natural Sciences of Japan, together with National Research Council (Canada), Ministry of Science and Technology (MOST; Taiwan), Academia Sinica Institute of Astronomy and Astrophysics (ASIAA; Taiwan), and Korea Astronomy and Space Science Institute (KASI; Republic of Korea), in cooperation with the Republic of Chile. The Joint ALMA Observatory is operated by ESO, Associated Universities, Inc. (AUI)/NRAO, and the National Astronomical Observatory of Japan (NAOJ). The National Radio Astronomy Observatory is a facility of the National Science Foundation operated under cooperative agreement by Associated Universities, Inc. The LMT is a project operated by the Instituto Nacional de Astrófisica, Óptica, y Electrónica (Mexico) and the University of Massachusetts at Amherst (USA). This work is partly based on observations carried out with the IRAM 30 m Telescope under project No. 084-17. The IRAM 30 m Telescope on Pico Veleta, Spain is operated by IRAM and supported by CNRS (Centre National de la Recherche Scientifique, France), MPG (Max-Planck-Gesellschaft, Germany), and IGN (Instituto Geográfico Nacional, Spain). This research has made use of NASA's Astrophysics Data System Bibliographic Services. Part of this research was carried out at the Jet Propulsion Laboratory, California Institute of Technology, under a contract with the National Aeronautics and Space Administration. The Event Horizon Telescope Collaboration thanks the following organizations and programs: the Academia Sinica; the Academy of Finland (projects 274477, 284495, 312496, and 315721); the Agencia Nacional de Investigación y Desarrollo (ANID), Chile via NCN19_058 (TITANs) and Fondecyt 1221421, the Alexander von Humboldt Stiftung; an Alfred P. Sloan Research Fellowship; Allegro, the European ALMA Regional Centre node in the Netherlands, the NL astronomy research network NOVA and the astronomy institutes of the University of Amsterdam, Leiden University and Radboud University; the ALMA North America Development Fund; the Astrophysics and High Energy Physics program by MCIN (with funding from European Union NextGenerationEU, PRTR-C17I1); the Black Hole Initiative, which is funded by grants from the John Templeton Foundation and the Gordon and Betty Moore Foundation (although the opinions expressed in this work are those of the author(s) and do not necessarily reflect the views of these Foundations); the Brinson Foundation; Chandra DD7-18089X and TM6-17006X; the China Scholarship Council; the China Postdoctoral Science Foundation fellowships (2020M671266, 2022M712084); Consejo Nacional de Ciencia y Tecnología (CONACYT, Mexico, projects U0004-246083, U0004-259839, F0003-272050, M0037-279006, F0003-281692, 104497, 275201, and 263356); the Consejería de Economía, Conocimiento, Empresas y Universidad of the Junta de Andalucía (grant P18-FR-1769), the Consejo Superior de Investigaciones Científicas (grant 2019AEP112); the Delaney Family via the Delaney Family John A. Wheeler Chair at Perimeter Institute; Dirección General de Asuntos del Personal Académico-Universidad Nacional Autónoma de México (DGAPA-UNAM, projects IN112417 and IN112820); the Dutch Organization for Scientific Research (NWO) for VICI award (grant 639.043.513), grant OCENW.KLEIN.113 and the Dutch black hole Consortium (with project No. NWA 1292.19.202) of the research program the National Science Agenda; the Dutch National Supercomputers, Cartesius and Snellius (NWO grant 2021.013); the EACOA Fellowship awarded by the East Asia Core Observatories Association, which consists of the Academia Sinica Institute of Astronomy and Astrophysics, the National Astronomical Observatory of Japan, Center for Astronomical Mega-Science, Chinese Academy of Sciences, and the Korea Astronomy and Space Science Institute; the European Union Horizon 2020 research and innovation program under grant agreements RadioNet (No 730562) and M2FINDERS (No 101018682); the Horizon ERC Grants 2021 program under grant agreement No. 101040021; the Generalitat Valenciana (grants APOSTD/2018/177 and ASFAE/2022/018) and GenT Program (project CIDEGENT/2018/021); MICINN Research Project PID2019-108995GB-C22; the European Research Council for advanced grant "JETSET: Launching, propagation and emission of relativistic jets from binary mergers and across mass scales" (grant No. 884631); the Institute for Advanced Study; the Istituto Nazionale di Fisica Nucleare (INFN) sezione di Napoli, iniziative specifiche TEONGRAV; the International Max Planck Research School for Astronomy and Astrophysics at the Universities of Bonn and Cologne; DFG research grant "Jet physics on horizon scales and beyond" (grant No. FR 4069/2-1); Joint Columbia/Flatiron Postdoctoral Fellowship, research at the Flatiron Institute is supported by the Simons Foundation; the Japan Ministry of Education, Culture, Sports, Science and Technology (MEXT; grant JPMXP1020200109); the Japan Society for the Promotion of Science (JSPS) Grant-in-Aid for JSPS Research Fellowship (JP17J08829); the Joint Institute for Computational Fundamental Science, Japan; the Key Research Program of Frontier Sciences, Chinese Academy of Sciences (CAS, grants QYZDJ-SSW-SLH057, QYZDJSSW-SYS008, ZDBS-LY-SLH011); the Leverhulme Trust Early Career Research Fellowship; the Max-Planck-Gesellschaft (MPG); the Max Planck Partner Group of the MPG and the CAS; the MEXT/JSPS KAKENHI (grants 18KK0090, JP21H01137, JP18H03721, JP18K13594, 18K03709, JP19K14761, 18H01245, 25120007); the Malaysian Fundamental Research Grant Scheme (FRGS) FRGS/1/2019/STG02/UM/02/6; the MIT International Science and Technology Initiatives (MISTI) Funds; the Ministry of Science and Technology (MOST) of Taiwan (103-2119-M-001-010-MY2, 105-2112-M-001-025-MY3, 105-2119-M-001-042, 106-2112-M-001-011, 106-2119-M-001-013, 106-2119-M-001-027, 106-2923-M-001-005, 107-2119-M-001-017, 107-2119-M-001-020, 107-2119-M-001-041, 107-2119-M-110-005, 107-2923-M-001-009, 108-2112-M-001-048, 108-2112-M-001-051, 108-2923-M-001-002, 109-2112-M-001-025, 109-2124-M-001-005, 109-2923-M-001-001, 110-2112-M-003-007-MY2, 110-2112-M-001-033, 110-2124-M-001-007, and 110-2923-M-001-001); the Ministry of Education (MoE) of Taiwan Yushan Young Scholar Program; the Physics Division, National Center for Theoretical Sciences of Taiwan; the National Aeronautics and Space Administration (NASA, Fermi Guest Investigator grant 80NSSC20K1567, NASA Astrophysics Theory Program grant 80NSSC20K0527, NASA NuSTAR award 80NSSC20K0645); NASA Hubble Fellowship grants HST-HF2-51431.001-A, HST-HF2-51482.001-A awarded by the Space Telescope Science Institute, which is operated by the Association of Universities for Research in Astronomy, Inc., for

NASA, under contract NAS5-26555; the National Institute of Natural Sciences (NINS) of Japan; the National Key Research and Development Program of China (grant 2016YFA0400704, 2017YFA0402703, 2016YFA0400702); the National Science Foundation (NSF, grants AST-0096454, AST-0352953, AST-0521233, AST-0705062, AST-0905844, AST-0922984, AST-1126433, AST-1140030, DGE-1144085, AST-1207704, AST-1207730, AST-1207752, MRI-1228509, OPP-1248097, AST-1310896, AST-1440254, AST-1555365, AST-1614868, AST-1615796, AST-1715061, AST-1716327, AST-1716536, OISE-1743747, AST-1816420, AST-1935980, AST-2034306); NSF Astronomy and Astrophysics Postdoctoral Fellowship (AST-1903847); the Natural Science Foundation of China (grants 11650110427, 10625314, 11721303, 11725312, 11873028, 11933007, 11991052, 11991053, 12192220, 12192223); the Natural Sciences and Engineering Research Council of Canada (NSERC, including a Discovery Grant and the NSERC Alexander Graham Bell Canada Graduate Scholarships-Doctoral Program); the National Youth Thousand Talents Program of China; the National Research Foundation of Korea (the Global PhD Fellowship Grant: grants NRF-2015H1A2A1033752, the Korea Research Fellowship Program: NRF-2015H1D3A1066561, Brain Pool Program: 2019H1D3A1A01102564, Basic Research Support Grant 2019R1F1A1059721, 2021R1A6A3A01086420, 2022R1C1C1005255); Netherlands Research School for Astronomy (NOVA) Virtual Institute of Accretion (VIA) postdoctoral fellowships; Onsala Space Observatory (OSO) national infrastructure, for the provisioning of its facilities/observational support (OSO receives funding through the Swedish Research Council under grant 2017-00648); the Perimeter Institute for Theoretical Physics (research at Perimeter Institute is supported by the Government of Canada through the Department of Innovation, Science and Economic Development and by the Province of Ontario through the Ministry of Research, Innovation and Science); the Princeton Gravity Initiative; the Spanish Ministerio de Ciencia e Innovación (grants PGC2018-098915-B-C21, AYA2016-80889-P, PID2019-108995GB-C21, and PID2020-117404GB-C21); the University of Pretoria for financial aid in the provision of the new Cluster Server nodes and SuperMicro (USA) for an SEEDING grant approved toward these nodes in 2020; the Shanghai Pilot Program for Basic Research, Chinese Academy of Science, Shanghai Branch (JCYJ-SHFY-2021-013); the State Agency for Research of the Spanish MCIU through the "Center of Excellence Severo Ochoa" award for the Instituto de Astrofísica de Andalucía (SEV-2017-0709); the Spinoza Prize SPI 78-409; the South African Research Chairs Initiative, through the South African Radio Astronomy Observatory (SARAO, grant ID 77948), which is a facility of the National Research Foundation (NRF), an agency of the Department of Science and Innovation (DSI) of South Africa; the Toray Science Foundation; the Swedish Research Council (VR); the US Department of Energy (USDOE) through the Los Alamos National Laboratory (operated by Triad National Security, LLC, for the National Nuclear Security Administration of the USDOE (contract 89233218CNA000001); and the YCAA Prize Postdoctoral Fellowship. This research used resources of the Oak Ridge Leadership Computing Facility at the Oak Ridge National Laboratory, which is supported by the Office of Science of the U.S. Department of Energy under contract No. DE-AC05-00OR22725. We also thank the Center for Computational Astrophysics, National Astronomical Observatory of Japan. The computing cluster of Shanghai VLBI correlator supported by the Special Fund for Astronomy from the Ministry of Finance in China is acknowledged. This work was partially supported by FAPESP (Fundação de Amparo á Pesquisa do Estado de São Paulo) under grant 2021/01183-8. APEX is a collaboration between the Max-Planck-Institut für Radioastronomie (Germany), ESO, and the Onsala Space Observatory (Sweden). The SMT is operated by the Arizona Radio Observatory, a part of the Steward Observatory of the University of Arizona, with financial support of operations from the State of Arizona and financial support for instrumentation development from the NSF. Support for SPT participation in the EHT is provided by the National Science Foundation through award OPP-1852617 to the University of Chicago. Partial support is also provided by the Kavli Institute of Cosmological Physics at the University of Chicago. The SPT hydrogen maser was provided on loan from the GLT, courtesy of ASIAA. The SMA is a joint project between the SAO and ASIAA and is funded by the Smithsonian Institution and the Academia Sinica. The JCMT is operated by the East Asian Observatory on behalf of the NAOJ, ASIAA, and KASI, as well as the Ministry of Finance of China, Chinese Academy of Sciences, and the National Key Research and Development Program (No. 2017YFA0402700) of China and Natural Science Foundation of China grant 11873028. Additional funding support for the JCMT is provided by the Science and Technologies Facility Council (UK) and participating universities in the UK and Canada. We acknowledge the significance that Maunakea, where the SMA and JCMT EHT stations are located, has for the indigenous Hawaiian people. The EHTC has received generous donations of FPGA chips from Xilinx Inc., under the Xilinx University Program. The EHTC has benefited from technology shared under an open-source license by the Collaboration for Astronomy Signal Processing and Electronics Research (CASPER). The EHT project is grateful to T4Science and Microsemi for their assistance with Hydrogen Masers. We gratefully acknowledge the support provided by the extended staff of the ALMA, both from the inception of the ALMA Phasing Project through the observational campaigns of 2017 and 2018. We would like to thank A. Deller and W. Brisken for EHT-specific support with the use of DiFX.

Facilities: ALMA, LMT, IRAM:30m.

Software: `MPIvdif2psrfits`, PRESTO (Ransom 2011), RIPTIDE (Morello et al. 2020), NUMPY (Harris et al. 2020), SCIPY (Virtanen et al. 2020), MATPLOTLIB (Hunter 2007), TEMPO (Nice et al. 2015), SIGPYPROC (Lorimer 2011).

Appendix
Details of Data Properties

In this Appendix we show example time series from the analyzed data of each of the three stations: phased ALMA, the LMT, and the IRAM 30 m Telescope. The data before and after the preparation and cleaning described in Section 2.2 are shown in Figures 6 and 7. Figure 6 presents a broader view, with several scans and a relatively large part of each observation (not necessarily all of it). In Figure 7 we show zoomed in versions, in which more details of the artifacts present in the data can be observed. Figure 7 also shows that the artifacts are not completely removed after the cleaning steps, but at least the most prominent undesired signals are reduced. Despite the residual artifacts remaining in the data, the pre-processing tests injecting synthetic pulsar signals in the data show that our algorithms are capable of finding pulsars if they exist (with sufficient strength) in the data (see Section 2.4). Some sensitivity to pulsars is certainly lost due to the particular noise characteristics of the data. We try to model and account for these losses in our analysis (see Sections 4.1 and 4.2).

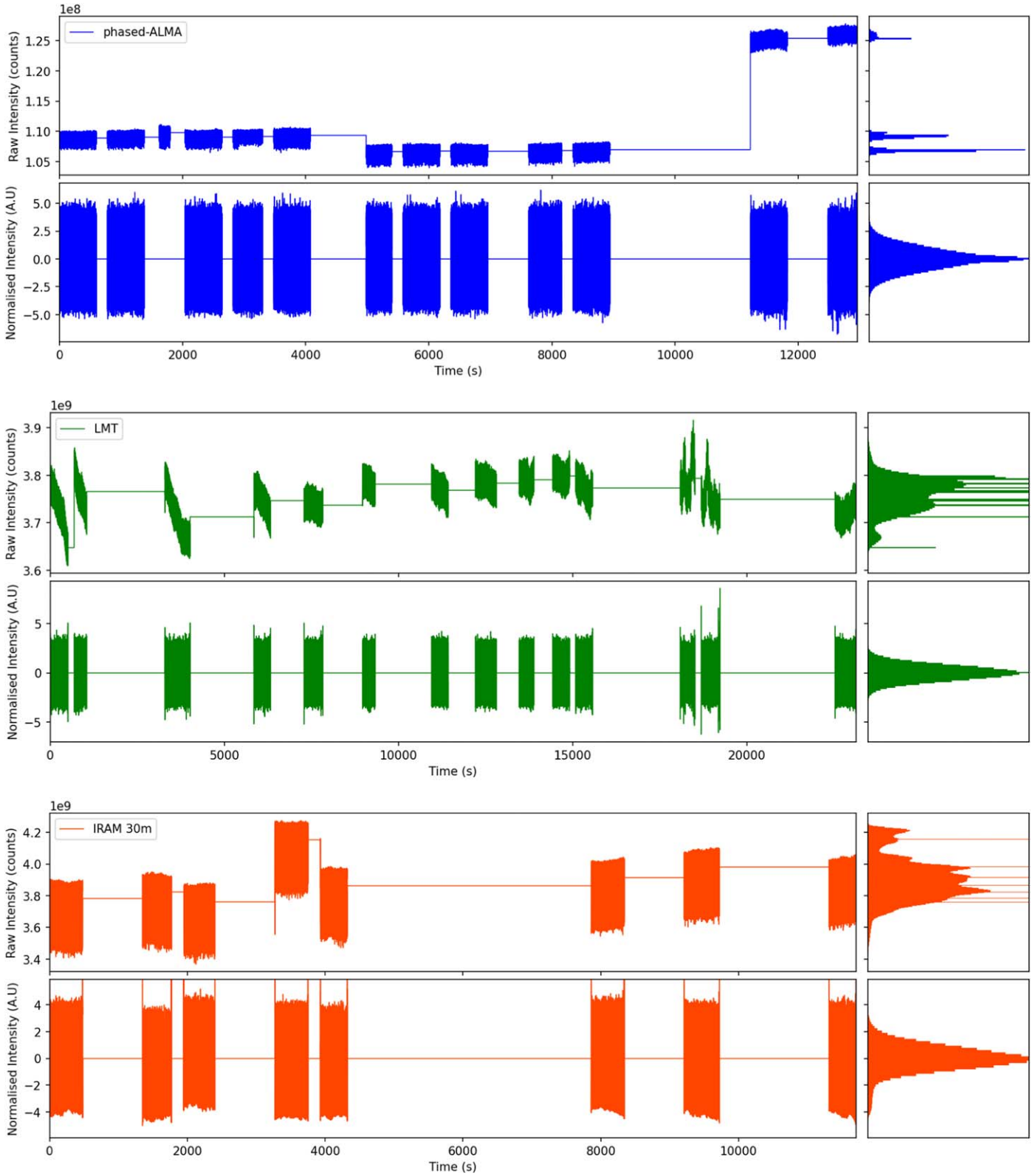

Figure 6. Example time series of the observations of Sgr A* analyzed in this paper. The top two panels corresponds to data from phased ALMA, the middle two panels to the LMT, and the bottom two panels to IRAM 30 m Telescope data. Each pair of panels corresponding to one station show the following: (top panels) the raw total intensity data just after the conversion to PSRFITS, and (bottom panels) the same total intensity time series after the preparation and cleaning described in Section 2.2. A description of the main features of the data from each station is presented in Section 2.2. The rightmost panels present a histogram of the distribution of the samples in linear scale. After the cleaning, the histograms tend to a Gaussian shape (although not perfect), indicating that the filtering and flagging schemes result in statistically better-behaved data.

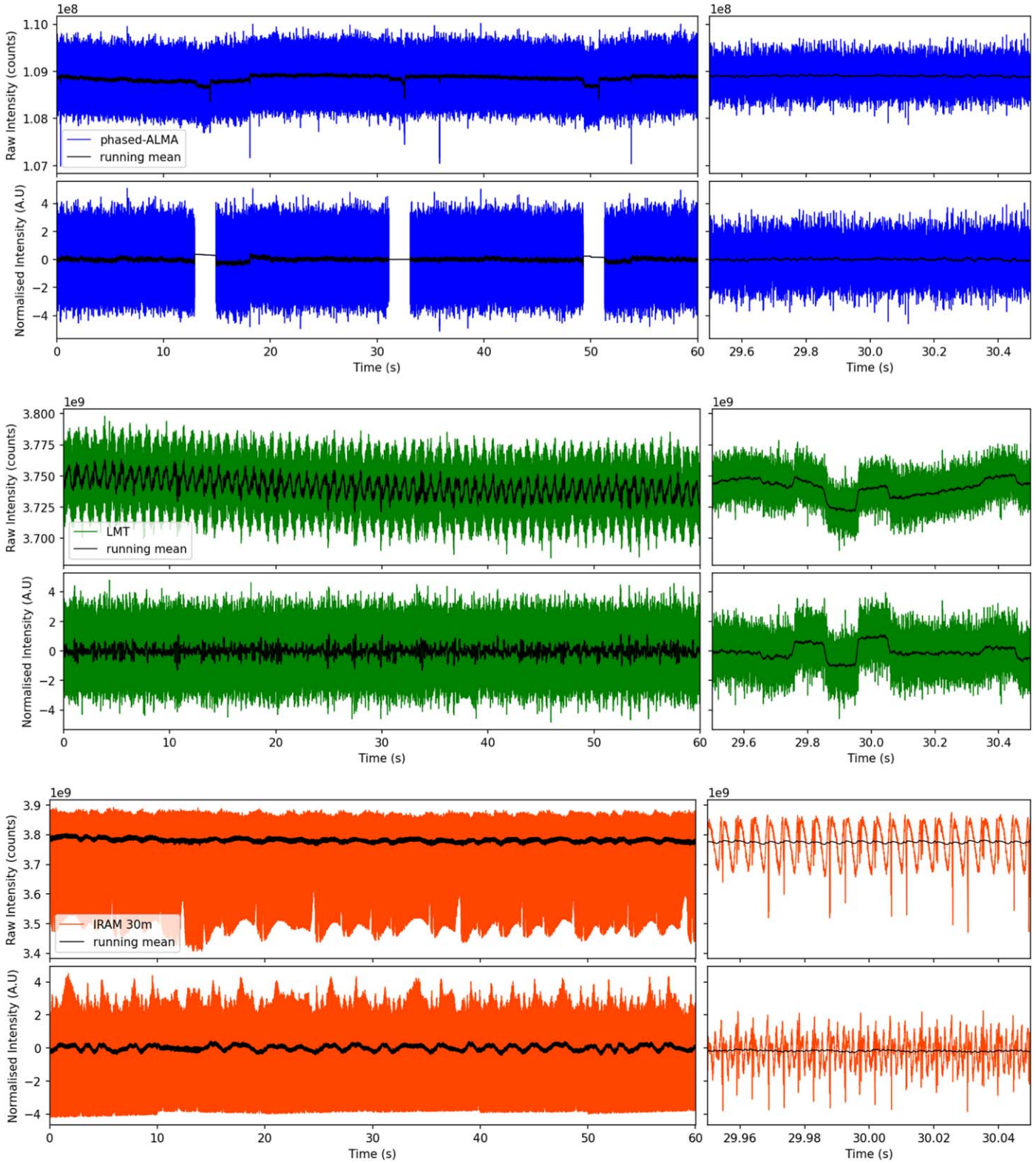

Figure 7. Zoom of the example time series of the observations of Sgr A* analyzed in this paper. The top two panels corresponds to data from phased ALMA, the middle two panels to the LMT, and the bottom two panels to IRAM 30 m Telescope data. Each pair of panels corresponding to one station show the following: (top panels) the raw total intensity data just after the conversion to PSRFITS, and (bottom panels) the same total intensity time series after the preparation and cleaning described in Section 2.2. A description of the main features of the data from each station is presented in Section 2.2. The panels on the right show an even closer zoom in, to facilitate the identification of the main issues of each data set. Note that for ALMA and LMT this extra zoom shows 1 s, while for the IRAM 30 m data, which suffer from much faster oscillations, the time axis of the right-hand panel encompasses only 0.1 s. The black solid line shows a running mean with resolution of 10 ms.

ORCID iDs

Pablo Torne https://orcid.org/0000-0001-8700-6058
Kuo Liu https://orcid.org/0000-0002-2953-7376
Ralph P. Eatough https://orcid.org/0000-0001-6196-4135
Jompoj Wongphechauxsorn https://orcid.org/0000-0002-7730-4956
James M. Cordes https://orcid.org/0000-0002-4049-1882
Gregory Desvignes https://orcid.org/0000-0003-3922-4055
Mariafelicia De Laurentis https://orcid.org/0000-0002-9945-682X
Michael Kramer https://orcid.org/0000-0002-4175-2271
Scott M. Ransom https://orcid.org/0000-0001-5799-9714
Shami Chatterjee https://orcid.org/0000-0002-2878-1502
Robert Wharton https://orcid.org/0000-0002-7416-5209
Ramesh Karuppusamy https://orcid.org/0000-0002-5307-2919
Lindy Blackburn https://orcid.org/0000-0002-9030-642X
Michael Janssen https://orcid.org/0000-0001-8685-6544
Chi-kwan Chan https://orcid.org/0000-0001-6337-6126
Geoffrey, B. Crew https://orcid.org/0000-0002-2079-3189
Lynn D. Matthews https://orcid.org/0000-0002-3728-8082
Ciriaco Goddi https://orcid.org/0000-0002-2542-7743
Helge Rottmann https://orcid.org/0000-0003-1799-8228
Jan Wagner https://orcid.org/0000-0003-1105-6109
Salvador Sánchez https://orcid.org/0000-0002-8042-5951
Ignacio Ruiz https://orcid.org/0000-0002-0965-5463
Federico Abbate https://orcid.org/0000-0002-9791-7661
Geoffrey C. Bower https://orcid.org/0000-0003-4056-9982
Juan J. Salamanca https://orcid.org/0000-0001-5704-2197
Arturo I. Gómez-Ruiz https://orcid.org/0000-0001-9395-1670
Alfredo Herrera-Aguilar https://orcid.org/0000-0003-4918-2231
Wu Jiang (江悟) https://orcid.org/0000-0001-7369-3539
Ru-Sen Lu (路如森) https://orcid.org/0000-0002-7692-7967
Ue-Li Pen https://orcid.org/0000-0003-2155-9578
Alexander W. Raymond https://orcid.org/0000-0002-5779-4767
Lijing Shao https://orcid.org/0000-0002-1334-8853
Zhiqiang Shen (沈志强) https://orcid.org/0000-0003-3540-8746
Miguel Sanchez-Portal https://orcid.org/0000-0003-0981-9664
Carsten Kramer https://orcid.org/0000-0002-4908-4925
Karl-Friedrich Schuster https://orcid.org/0000-0003-2890-9454
Michael D. Johnson https://orcid.org/0000-0002-4120-3029
Kazi L. J. Rygl https://orcid.org/0000-0003-4146-9043
Kazunori Akiyama https://orcid.org/0000-0002-9475-4254
Antxon Alberdi https://orcid.org/0000-0002-9371-1033
Juan Carlos Algaba https://orcid.org/0000-0001-6993-1696
Richard Anantua https://orcid.org/0000-0003-3457-7660
Keiichi Asada https://orcid.org/0000-0001-6988-8763
Rebecca Azulay https://orcid.org/0000-0002-2200-5393
Uwe Bach https://orcid.org/0000-0002-7722-8412
Anne-Kathrin Baczko https://orcid.org/0000-0003-3090-3975
Mislav Baloković https://orcid.org/0000-0003-0476-6647
John Barrett https://orcid.org/0000-0002-9290-0764
Michi Bauböck https://orcid.org/0000-0002-5518-2812
Bradford A. Benson https://orcid.org/0000-0002-5108-6823
Raymond Blundell https://orcid.org/0000-0002-5929-5857
Katherine L. Bouman https://orcid.org/0000-0003-0077-4367
Hope Boyce https://orcid.org/0000-0002-6530-5783
Christiaan D. Brinkerink https://orcid.org/0000-0002-2322-0749
Roger Brissenden https://orcid.org/0000-0002-2556-0894
Silke Britzen https://orcid.org/0000-0001-9240-6734
Avery E. Broderick https://orcid.org/0000-0002-3351-760X
Dominique Broguiere https://orcid.org/0000-0001-9151-6683
Thomas Bronzwaer https://orcid.org/0000-0003-1151-3971
Sandra Bustamante https://orcid.org/0000-0001-6169-1894
Do-Young Byun https://orcid.org/0000-0003-1157-4109
John E. Carlstrom https://orcid.org/0000-0002-2044-7665
Chiara Ceccobello https://orcid.org/0000-0002-4767-9925
Andrew Chael https://orcid.org/0000-0003-2966-6220
Dominic O. Chang https://orcid.org/0000-0001-9939-5257
Koushik Chatterjee https://orcid.org/0000-0002-2825-3590
Ming-Tang Chen https://orcid.org/0000-0001-6573-3318
Yongjun Chen (陈永军) https://orcid.org/0000-0001-5650-6770
Xiaopeng Cheng https://orcid.org/0000-0003-4407-9868
Ilje Cho https://orcid.org/0000-0001-6083-7521
Pierre Christian https://orcid.org/0000-0001-6820-9941
Nicholas S. Conroy https://orcid.org/0000-0003-2886-2377
John E. Conway https://orcid.org/0000-0003-2448-9181
Thomas M. Crawford https://orcid.org/0000-0001-9000-5013
Alejandro Cruz-Osorio https://orcid.org/0000-0002-3945-6342
Yuzhu Cui (崔玉竹) https://orcid.org/0000-0001-6311-4345
Rohan Dahale https://orcid.org/0000-0001-6982-9034
Jordy Davelaar https://orcid.org/0000-0002-2685-2434
Roger Deane https://orcid.org/0000-0003-1027-5043
Jessica Dempsey https://orcid.org/0000-0003-1269-9667
Jason Dexter https://orcid.org/0000-0003-3903-0373
Vedant Dhruv https://orcid.org/0000-0001-6765-877X
Sheperd S. Doeleman https://orcid.org/0000-0002-9031-0904
Sean Dougal https://orcid.org/0000-0002-3769-1314
Sergio A. Dzib https://orcid.org/0000-0001-6010-6200
Razieh Emami https://orcid.org/0000-0002-2791-5011
Heino Falcke https://orcid.org/0000-0002-2526-6724
Joseph Farah https://orcid.org/0000-0003-4914-5625
Vincent L. Fish https://orcid.org/0000-0002-7128-9345
Ed Fomalont https://orcid.org/0000-0002-9036-2747
H. Alyson Ford https://orcid.org/0000-0002-9797-0972
Marianna Foschi https://orcid.org/0000-0001-8147-4993
Raquel Fraga-Encinas https://orcid.org/0000-0002-5222-1361
Per Friberg https://orcid.org/0000-0002-8010-8454
Christian M. Fromm https://orcid.org/0000-0002-1827-1656
Antonio Fuentes https://orcid.org/0000-0002-8773-4933
Peter Galison https://orcid.org/0000-0002-6429-3872
Charles F. Gammie https://orcid.org/0000-0001-7451-8935
Roberto García https://orcid.org/0000-0002-6584-7443
Olivier Gentaz https://orcid.org/0000-0002-0115-4605
Boris Georgiev https://orcid.org/0000-0002-3586-6424
Roman Gold https://orcid.org/0000-0003-2492-1966
José L. Gómez https://orcid.org/0000-0003-4190-7613
Minfeng Gu (顾敏峰) https://orcid.org/0000-0002-4455-6946
Mark Gurwell https://orcid.org/0000-0003-0685-3621
Kazuhiro Hada https://orcid.org/0000-0001-6906-772X
Daryl Haggard https://orcid.org/0000-0001-6803-2138
Michael H. Hecht https://orcid.org/0000-0002-4114-4583
Ronald Hesper https://orcid.org/0000-0003-1918-6098
Dirk Heumann https://orcid.org/0000-0002-7671-0047
Luis C. Ho (何子山) https://orcid.org/0000-0001-6947-5846
Paul Ho https://orcid.org/0000-0002-3412-4306
Mareki Honma https://orcid.org/0000-0003-4058-9000
Chih-Wei L. Huang https://orcid.org/0000-0001-5641-3953
Lei Huang (黄磊) https://orcid.org/0000-0002-1923-227X
Shiro Ikeda https://orcid.org/0000-0002-2462-1448

C. M. Violette Impellizzeri https://orcid.org/0000-0002-3443-2472
Makoto Inoue https://orcid.org/0000-0001-5037-3989
Sara Issaoun https://orcid.org/0000-0002-5297-921X
David J. James https://orcid.org/0000-0001-5160-4486
Buell T. Jannuzi https://orcid.org/0000-0002-1578-6582
Britton Jeter https://orcid.org/0000-0003-2847-1712
Alejandra Jiménez-Rosales https://orcid.org/0000-0002-2662-3754
Svetlana Jorstad https://orcid.org/0000-0001-6158-1708
Abhishek V. Joshi https://orcid.org/0000-0002-2514-5965
Taehyun Jung https://orcid.org/0000-0001-7003-8643
Mansour Karami https://orcid.org/0000-0001-7387-9333
Tomohisa Kawashima https://orcid.org/0000-0001-8527-0496
Garrett K. Keating https://orcid.org/0000-0002-3490-146X
Mark Kettenis https://orcid.org/0000-0002-6156-5617
Dong-Jin Kim https://orcid.org/0000-0002-7038-2118
Jae-Young Kim https://orcid.org/0000-0001-8229-7183
Jongsoo Kim https://orcid.org/0000-0002-1229-0426
Junhan Kim https://orcid.org/0000-0002-4274-9373
Motoki Kino https://orcid.org/0000-0002-2709-7338
Jun Yi Koay https://orcid.org/0000-0002-7029-6658
Prashant Kocherlakota https://orcid.org/0000-0001-7386-7439
Shoko Koyama https://orcid.org/0000-0002-3723-3372
Thomas P. Krichbaum https://orcid.org/0000-0002-4892-9586
Cheng-Yu Kuo https://orcid.org/0000-0001-6211-5581
Noemi La Bella https://orcid.org/0000-0002-8116-9427
Tod R. Lauer https://orcid.org/0000-0003-3234-7247
Daeyoung Lee https://orcid.org/0000-0002-3350-5588
Sang-Sung Lee https://orcid.org/0000-0002-6269-594X
Po Kin Leung https://orcid.org/0000-0002-8802-8256
Aviad Levis https://orcid.org/0000-0001-7307-632X
Zhiyuan Li (李志远) https://orcid.org/0000-0003-0355-6437
Rocco Lico https://orcid.org/0000-0001-7361-2460
Greg Lindahl https://orcid.org/0000-0002-6100-4772
Michael Lindqvist https://orcid.org/0000-0002-3669-0715
Mikhail Lisakov https://orcid.org/0000-0001-6088-3819
Jun Liu (刘俊) https://orcid.org/0000-0002-7615-7499
Elisabetta Liuzzo https://orcid.org/0000-0003-0995-5201
Wen-Ping Lo https://orcid.org/0000-0003-1869-2503
Andrei P. Lobanov https://orcid.org/0000-0003-1622-1484
Laurent Loinard https://orcid.org/0000-0002-5635-3345
Colin J. Lonsdale https://orcid.org/0000-0003-4062-4654
Nicholas R. MacDonald https://orcid.org/0000-0002-6684-8691
Jirong Mao (毛基荣) https://orcid.org/0000-0002-7077-7195
Nicola Marchili https://orcid.org/0000-0002-5523-7588
Sera Markoff https://orcid.org/0000-0001-9564-0876
Daniel P. Marrone https://orcid.org/0000-0002-2367-1080
Alan P. Marscher https://orcid.org/0000-0001-7396-3332
Iván Martí-Vidal https://orcid.org/0000-0003-3708-9611
Satoki Matsushita https://orcid.org/0000-0002-2127-7880
Lia Medeiros https://orcid.org/0000-0003-2342-6728
Karl M. Menten https://orcid.org/0000-0001-6459-0669
Daniel Michalik https://orcid.org/0000-0002-7618-6556
Izumi Mizuno https://orcid.org/0000-0002-7210-6264
Yosuke Mizuno https://orcid.org/0000-0002-8131-6730
James M. Moran https://orcid.org/0000-0002-3882-4414
Kotaro Moriyama https://orcid.org/0000-0003-1364-3761
Monika Moscibrodzka https://orcid.org/0000-0002-4661-6332
Cornelia Müller https://orcid.org/0000-0002-2739-2994
Hendrik Müller https://orcid.org/0000-0002-9250-0197
Alejandro Mus https://orcid.org/0000-0003-0329-6874
Gibwa Musoke https://orcid.org/0000-0003-1984-189X
Ioannis Myserlis https://orcid.org/0000-0003-3025-9497
Andrew Nadolski https://orcid.org/0000-0001-9479-9957
Hiroshi Nagai https://orcid.org/0000-0003-0292-3645
Neil M. Nagar https://orcid.org/0000-0001-6920-662X
Masanori Nakamura https://orcid.org/0000-0001-6081-2420
Ramesh Narayan https://orcid.org/0000-0002-1919-2730
Gopal Narayanan https://orcid.org/0000-0002-4723-6569
Iniyan Natarajan https://orcid.org/0000-0001-8242-4373
Joey Neilsen https://orcid.org/0000-0002-8247-786X
Roberto Neri https://orcid.org/0000-0002-7176-4046
Chunchong Ni https://orcid.org/0000-0003-1361-5699
Aristeidis Noutsos https://orcid.org/0000-0002-4151-3860
Michael A. Nowak https://orcid.org/0000-0001-6923-1315
Junghwan Oh https://orcid.org/0000-0002-4991-9638
Hiroki Okino https://orcid.org/0000-0003-3779-2016
Héctor Olivares https://orcid.org/0000-0001-6833-7580
Gisela N. Ortiz-León https://orcid.org/0000-0002-2863-676X
Tomoaki Oyama https://orcid.org/0000-0003-4046-2923
Feryal Özel https://orcid.org/0000-0003-4413-1523
Daniel C. M. Palumbo https://orcid.org/0000-0002-7179-3816
Georgios Filippos Paraschos https://orcid.org/0000-0001-6757-3098
Jongho Park https://orcid.org/0000-0001-6558-9053
Harriet Parsons https://orcid.org/0000-0002-6327-3423
Nimesh Patel https://orcid.org/0000-0002-6021-9421
Dominic W. Pesce https://orcid.org/0000-0002-5278-9221
Richard Plambeck https://orcid.org/0000-0001-6765-9609
Oliver Porth https://orcid.org/0000-0002-4584-2557
Felix M. Pötzl https://orcid.org/0000-0002-6579-8311
Ben Prather https://orcid.org/0000-0002-0393-7734
Jorge A. Preciado-López https://orcid.org/0000-0002-4146-0113
Dimitrios Psaltis https://orcid.org/0000-0003-1035-3240
Hung-Yi Pu https://orcid.org/0000-0001-9270-8812
Venkatessh Ramakrishnan https://orcid.org/0000-0002-9248-086X
Ramprasad Rao https://orcid.org/0000-0002-1407-7944
Mark G. Rawlings https://orcid.org/0000-0002-6529-202X
Luciano Rezzolla https://orcid.org/0000-0002-1330-7103
Angelo Ricarte https://orcid.org/0000-0001-5287-0452
Bart Ripperda https://orcid.org/0000-0002-7301-3908
Freek Roelofs https://orcid.org/0000-0001-5461-3687
Alan Rogers https://orcid.org/0000-0003-1941-7458
Eduardo Ros https://orcid.org/0000-0001-9503-4892
Cristina Romero-Cañizales https://orcid.org/0000-0001-6301-9073
Arash Roshanineshat https://orcid.org/0000-0002-8280-9238
Alan L. Roy https://orcid.org/0000-0002-1931-0135
Chet Ruszczyk https://orcid.org/0000-0001-7278-9707
David Sánchez-Argüelles https://orcid.org/0000-0002-7344-9920
Mahito Sasada https://orcid.org/0000-0001-5946-9960
Kaushik Satapathy https://orcid.org/0000-0003-0433-3585
Tuomas Savolainen https://orcid.org/0000-0001-6214-1085
Jonathan Schonfeld https://orcid.org/0000-0002-8909-2401
Des Small https://orcid.org/0000-0003-3723-5404
Bong Won Sohn https://orcid.org/0000-0002-4148-8378
Jason SooHoo https://orcid.org/0000-0003-1938-0720
Kamal Souccar https://orcid.org/0000-0001-7915-5272
He Sun (孙赫) https://orcid.org/0000-0003-1526-6787
Alexandra J. Tetarenko https://orcid.org/0000-0003-3906-4354
Paul Tiede https://orcid.org/0000-0003-3826-5648
Remo P. J. Tilanus https://orcid.org/0000-0002-6514-553X
Michael Titus https://orcid.org/0000-0001-9001-3275

Teresa Toscano https://orcid.org/0000-0003-3658-7862
Efthalia Traianou https://orcid.org/0000-0002-1209-6500
Tyler Trent https://orcid.org/0009-0004-8116-3123
Sascha Trippe https://orcid.org/0000-0003-0465-1559
Matthew Turk https://orcid.org/0000-0002-5294-0198
Ilse van Bemmel https://orcid.org/0000-0001-5473-2950
Huib Jan van Langevelde https://orcid.org/0000-0002-0230-5946
Daniel R. van Rossum https://orcid.org/0000-0001-7772-6131
Jesse Vos https://orcid.org/0000-0003-3349-7394
Derek Ward-Thompson https://orcid.org/0000-0003-1140-2761
John Wardle https://orcid.org/0000-0002-8960-2942
Jonathan Weintroub https://orcid.org/0000-0002-4603-5204
Norbert Wex https://orcid.org/0000-0003-4058-2837
Maciek Wielgus https://orcid.org/0000-0002-8635-4242
Kaj Wiik https://orcid.org/0000-0002-0862-3398
Gunther Witzel https://orcid.org/0000-0003-2618-797X
Michael F. Wondrak https://orcid.org/0000-0002-6894-1072
George N. Wong https://orcid.org/0000-0001-6952-2147
Qingwen Wu (吴庆文) https://orcid.org/0000-0003-4773-4987
Nitika Yadlapalli https://orcid.org/0000-0003-3255-4617
Paul Yamaguchi https://orcid.org/0000-0002-6017-8199
Aristomenis Yfantis https://orcid.org/0000-0002-3244-7072
Doosoo Yoon https://orcid.org/0000-0001-8694-8166
André Young https://orcid.org/0000-0003-0000-2682
Ken Young https://orcid.org/0000-0002-3666-4920
Ziri Younsi https://orcid.org/0000-0001-9283-1191
Wei Yu (于威) https://orcid.org/0000-0002-5168-6052
Feng Yuan (袁峰) https://orcid.org/0000-0003-3564-6437
Ye-Fei Yuan (袁业飞) https://orcid.org/0000-0002-7330-4756
J. Anton Zensus https://orcid.org/0000-0001-7470-3321
Shuo Zhang https://orcid.org/0000-0002-2967-790X
Guang-Yao Zhao https://orcid.org/0000-0002-4417-1659
Shan-Shan Zhao (赵杉杉) https://orcid.org/0000-0002-9774-3606

References

Abbott, B. P., Abbott, R., Abbott, T. D., et al. 2016, PhRvL, 116, 061102
Ajello, M., Albert, A., Atwood, W. B., et al. 2016, ApJ, 819, 44
Alexander, T. 2017, ARA&A, 55, 17
Andersen, B. C., & Ransom, S. M. 2018, ApJL, 863, L13
Bagchi, M., Lorimer, D. R., & Wolfe, S. 2013, MNRAS, 432, 1303
Bailes, M., Johnston, S., Bell, J. F., et al. 1997, ApJ, 481, 386
Balakrishnan, V., Champion, D., Barr, E., et al. 2022, MNRAS, 511, 1265
Bartels, R., Krishnamurthy, S., & Weniger, C. 2016, PhRvL, 116, 051102
Bassa, C. G., Janssen, G. H., Karuppusamy, R., et al. 2016, MNRAS, 456, 2196
Bates, S. D., Lorimer, D. R., & Verbiest, J. P. W. 2013, MNRAS, 431, 1352
Baumgardt, H., Amaro-Seoane, P., & Schödel, R. 2018, A&A, 609, A28
Blandford, R. D., & Scharlemann, E. T. 1976, MNRAS, 174, 59
Bower, G. C., Deller, A., Demorest, P., et al. 2014, ApJL, 780, L2
Bower, G. C., Deller, A., Demorest, P., et al. 2015, ApJ, 798, 120
Bower, G. C., Chatterjee, S., Cordes, J., et al. 2018, in ASP Conf. Ser. 517, Science with a Next Generation Very Large Array, ed. Eric Murphy (San Francisco, CA: ASP), 793
Cameron, A. D., Barr, E. D., Champion, D. J., Kramer, M., & Zhu, W. W. 2017, MNRAS, 468, 1994
Camilo, F., Ransom, S. M., Peñalver, J., et al. 2007, ApJ, 669, 561
Chen, Z., Do, T., Ghez, A. M., et al. 2023, ApJ, 944, 79
Chennamangalam, J., & Lorimer, D. R. 2014, MNRAS, 440, L86
Chu, C.-Y., Ng, C. Y., Kong, A. K. H., & Chang, H.-K. 2021, MNRAS, 503, 1214
Cooper, B. F. C. 1970, AuJPh, 23, 521
Cordes, J. M., & Chernoff, D. F. 1997, ApJ, 482, 971
Cordes, J. M., & Lazio, J. T. W. 1997, ApJ, 475, 557
Cordes, J. M., & Lazio, T. J. W. 2002, arXiv:astro-ph/0207156
Cordes, J. M., & McLaughlin, M. A. 2003, ApJ, 596, 1142
Daylan, T., Finkbeiner, D. P., Hooper, D., et al. 2016, PDU, 12, 1
Deneva, J. S., Cordes, J. M., & Lazio, T. J. W. 2009, ApJL, 702, L177
Desvignes, G., Eatough, R. P., Pen, U. L., et al. 2018, ApJL, 852, L12
Dexter, J., Deller, A., Bower, G. C., et al. 2017, MNRAS, 471, 3563
Dexter, J., & O'Leary, R. M. 2014, ApJL, 783, L7
Do, T., Hees, A., Ghez, A., et al. 2019, Sci, 365, 664
Eatough, R. P., Falcke, H., Karuppusamy, R., et al. 2013, Natur, 501, 391
Eatough, R. P., Torne, P., Desvignes, G., et al. 2021, MNRAS, 507, 5053
Event Horizon Telescope Collaboration, Akiyama, K., Alberdi, A., et al. 2019a, ApJL, 875, L1
Event Horizon Telescope Collaboration, Akiyama, K., Alberdi, A., et al. 2019b, ApJL, 875, L5
Event Horizon Telescope Collaboration, Akiyama, K., Alberdi, A., et al. 2019c, ApJL, 875, L6
Event Horizon Telescope Collaboration, Akiyama, K., Alberdi, A., et al. 2019d, ApJL, 875, L2
Event Horizon Telescope Collaboration, Akiyama, K., Alberdi, A., et al. 2019e, ApJL, 875, L3
Event Horizon Telescope Collaboration, Akiyama, K., Alberdi, A., et al. 2022a, ApJL, 930, L12
Event Horizon Telescope Collaboration, Akiyama, K., Alberdi, A., et al. 2022b, ApJL, 930, L17
Event Horizon Telescope Collaboration, Akiyama, K., Alberdi, A., et al. 2022c, ApJL, 930, L13
Faucher-Giguère, C.-A., & Kaspi, V. M. 2006, ApJ, 643, 332
Figer, D. F. 2009, in Massive Stars: From Pop III and GRBs to the Milky Way, ed. M. Livio & E. Villaver (Cambridge: Cambridge Univ. Press), 40
Freire, P. C. C. 2005, in ASP Conf. Ser. 328, Binary Radio Pulsars, ed. F. A. Rasio & I. H. Stairs (San Francisco, CA: ASP), 405
Gillessen, S., Plewa, P. M., Eisenhauer, F., et al. 2017, ApJ, 837, 30
Goddi, C., Martí-Vidal, I., Messias, H., et al. 2019, PASP, 131, 075003
Goddi, C., Martí-Vidal, I., Messias, H., et al. 2021, ApJL, 910, L14
Gordon, C., & Macias, O. 2013, PhRvD, 88, 083521
Gravity Collaboration, Abuter, R., Amorim, A., et al. 2018, A&A, 615, L15
Gravity Collaboration, Abuter, R., Amorim, A., et al. 2019, A&A, 625, L10
Gravity Collaboration, Abuter, R., Amorim, A., et al. 2020, A&A, 636, L5
Gravity Collaboration, Abuter, R., Amorim, A., et al. 2021, A&A, 647, A59
Harris, C. R., Millman, K. J., van der Walt, S. J., et al. 2020, Natur, 585, 357
Hotan, A. W., van Straten, W., & Manchester, R. N. 2004, PASA, 21, 302
Hunter, J. D. 2007, CSE, 9, 90
Jankowski, F., van Straten, W., Keane, E. F., et al. 2018, MNRAS, 473, 4436
Johnston, S., Kramer, M., Lorimer, D. R., et al. 2006, MNRAS, 373, L6
Karako-Argaman, C., Kaspi, V. M., Lynch, R. S., et al. 2015, ApJ, 809, 67
Keane, E. F., & Kramer, M. 2008, MNRAS, 391, 2009
Keane, E. F., Kramer, M., Lyne, A. G., Stappers, B. W., & McLaughlin, M. A. 2011, MNRAS, 415, 3065
Kennea, J. A., Burrows, D. N., Kouveliotou, C., et al. 2013, ApJL, 770, L24
Kramer, M. 1998, ApJ, 509, 856
Kramer, M., Backer, D. C., Cordes, J. M., et al. 2004, NewAR, 48, 993
Kramer, M., Xilouris, K. M., Lorimer, D. R., et al. 1998, ApJ, 501, 270
Lazarus, P., Brazier, A., Hessels, J. W. T., et al. 2015, ApJ, 812, 81
Liu, K. 2012, PhD thesis, Univ. Manchester
Liu, K., Desvignes, G., Eatough, R. P., et al. 2021, ApJ, 914, 30
Liu, K., Eatough, R. P., Wex, N., & Kramer, M. 2014, MNRAS, 445, 3115
Liu, K., Wex, N., Kramer, M., Cordes, J. M., & Lazio, T. J. W. 2012, ApJ, 747, 1
Liu, K., Young, A., Wharton, R., et al. 2019, ApJL, 885, L10
Löhmer, O., Jessner, A., Kramer, M., Wielebinski, R., & Maron, O. 2008, A&A, 480, 623
Lorimer, D. R., 2011 SIGPROC: Pulsar Signal Processing Programs, Astrophysics Source Code Library, ascl:1107.016
Lorimer, D. R., & Kramer, M. 2004, Handbook of Pulsar Astronomy, Vol. 4 (Cambridge: Cambridge Univ. Press)
Lyne, A. G. 2003, in ASP Conf. Ser. 302, The Development of Pulsar Search Techniques, ed. M. Bailes, D. J. Nice, & S. E. Thorsett (San Francisco, CA: ASP), 11
Macquart, J.-P., & Kanekar, N. 2015, ApJ, 805, 172
Macquart, J.-P., Kanekar, N., Frail, D. A., & Ransom, S. M. 2010, ApJ, 715, 939
Manchester, R. N., Hobbs, G. B., Teoh, A., & Hobbs, M. 2005, AJ, 129, 1993
Maron, O., Kijak, J., Kramer, M., & Wielebinski, R. 2000, A&AS, 147, 195
McLaughlin, M. A., & Cordes, J. M. 2003, ApJ, 596, 982
Mizuno, Y., Younsi, Z., Fromm, C. M., et al. 2018, NatAs, 2, 585
Morello, V., Barr, E. D., Stappers, B. W., Keane, E. F., & Lyne, A. G. 2020, MNRAS, 497, 4654
Morris, M. R. 2023, in Proc. 7th Chile-Cologne-Bonn Symp., Physics and Chemistry of Star Formation: The Dynamical ISM Across Time and Spatial Scales, ed. V. Ossenkopf-Okada et al. (Köln: Universitäts- und Stadtbibliothekj Köln), 49

Mus, A., Martí-Vidal, I., Wielgus, M., & Stroud, G. 2022, A&A, 666, A39
Ng, C., Champion, D. J., Bailes, M., et al. 2015, MNRAS, 450, 2922
Nice, D., Demorest, P., Stairs, I., et al., 2015 Tempo: Pulsar timing data analysis, Astrophysics Source Code Library, ascl:1509.002
Nogueras-Lara, F., Schödel, R., & Neumayer, N. 2022, NatAs, 6, 1178
Özel, F., Psaltis, D., & Younsi, Z. 2022, ApJ, 941, 88
Perera, B. B. P., McLaughlin, M. A., Kramer, M., et al. 2010, ApJ, 721, 1193
Pfahl, E., & Loeb, A. 2004, ApJ, 615, 253
Pfuhl, O., Fritz, T. K., Zilka, M., et al. 2011, ApJ, 741, 108
Philippov, A., & Kramer, M. 2022, ARA&A, 60, 495
Psaltis, D., Medeiros, L., Christian, P., et al. 2020, PhRvL, 125, 141104
Psaltis, D., Wex, N., & Kramer, M. 2016, ApJ, 818, 121
Rajwade, K. M., Lorimer, D. R., & Anderson, L. D. 2017, MNRAS, 471, 730
Ransom, S., 2011 PRESTO: PulsaR Exploration and Search TOolkit, Astrophysics Source Code Library, ascl:1107.017
Ransom, S. M. 2001, PhD thesis, Harvard Univ.
Ransom, S. M., Eikenberry, S. S., & Middleditch, J. 2002, AJ, 124, 1788
Rea, N., Esposito, P., Pons, J. A., et al. 2013, ApJL, 775, L34
Sabha, N., Eckart, A., Merritt, D., et al. 2012, A&A, 545, A70
Sartore, N., Ripamonti, E., Treves, A., & Turolla, R. 2010, A&A, 510, A23
Schnitzeler, D. H. F. M., Eatough, R. P., Ferrière, K., et al. 2016, MNRAS, 459, 3005
Schödel, R., Nogueras-Lara, F., Gallego-Cano, E., et al. 2020, A&A, 641, A102
Singh, S., Roy, J., Panda, U., et al. 2022, ApJ, 934, 138
Spitler, L. G., Lee, K. J., Eatough, R. P., et al. 2014, ApJL, 780, L3
Staelin, D. H. 1969, IEEEP, 57, 724
Suresh, A., Cordes, J. M., Chatterjee, S., et al. 2022, ApJ, 933, 121
Taylor, J. H., & Weisberg, J. M. 1982, ApJ, 253, 908
Taylor, J. H., & Weisberg, J. M. 1989, ApJ, 345, 434
Torne, P., Bell, G. S., Bintley, D., et al. 2022, ApJL, 925, L17
Torne, P., Desvignes, G., Eatough, R. P., et al. 2017, MNRAS, 465, 242
Torne, P., Desvignes, G., Eatough, R. P., et al. 2021, A&A, 650, A95
Torne, P., Eatough, R. P., Karuppusamy, R., et al. 2015, MNRAS, 451, L50
Torne, P., Macías-Pérez, J., Ladjelate, B., et al. 2020, A&A, 640, L2
Virtanen, P., Gommers, R., Oliphant, T. E., et al. 2020, NatMe, 17, 261
Weinberg, N. N., Milosavljević, M., & Ghez, A. M. 2005, ApJ, 622, 878
Wex, N., & Kopeikin, S. M. 1999, ApJ, 514, 388
Wex, N., & Kramer, M. 2020, Univ, 6, 156
Wharton, R. S., Chatterjee, S., Cordes, J. M., Deneva, J. S., & Lazio, T. J. W. 2012, ApJ, 753, 108
Wongphechauxsorn, J. 2024, MNRAS, 527, 3208
Younsi, Z., Psaltis, D., & Özel, F. 2023, ApJ, 942, 47